

CFD Verification of Supersonic Retropropulsion for a Central and Peripheral Configuration

Christopher E. Cordell, Jr., Ian G. Clark, Robert D. Braun
Georgia Institute of Technology
270 Ferst Drive
Atlanta, GA 30363
404-894-7783
chris.cordell@gatech.edu

Abstract—Supersonic retropropulsion (SRP) is a potential enabling technology for deceleration of high mass vehicles at Mars. Previous sub-scale testing, performed during the 1960s and 1970s to explore and characterize various decelerator technologies, focused on SRP configurations with a single central nozzle located along the axis of a vehicle; however, some multiple nozzle configurations were examined. Only one of these tests showed a peripheral configuration with nozzles outboard of the vehicle centerline. Recent computational efforts have been initiated to examine the capability of computational fluid dynamics (CFD) to capture the complex SRP flow fields. This study assesses the accuracy of a CFD tool over a range of thrust conditions for both a central and peripheral configuration. Included is a discussion of the agreement between the CFD simulations and available wind tunnel data as well as a discussion of computational impacts on SRP simulation.

Supersonic retropropulsion was an area of interest for deceleration as early as the 1960s and early 1970s prior to the Viking missions. Preliminary wind tunnel tests explored the effects of retropropulsion on the aerodynamics of the entry body for a variety of geometries and nozzle configurations. Nozzle configurations for these tests primarily fall into one of two categories. One is a central configuration with a single nozzle oriented along the axis of a blunt body, and the other is a peripheral configuration where multiple nozzles are offset from the centerline and distributed circularly.

For the central configuration, tests run on a 60° sphere cone [2] and 70° sphere cone [3] consistently show that as thrust increases, surface pressure along the forebody decreases. The thrust from the nozzle provides increased deceleration force at the expense of the aerodynamic drag resulting from the pressure along the body. Both of these tests also show distinct flow structure regimes for varying thrust conditions. The regimes are generally characterized by an unsteady flow structure for low thrust values, with increasing thrust eventually creating a steady flow field. Both tests determine that the transition between the regimes is a function of the jet pressure relative to the freestream pressure. A more recent test investigated the effects of a single nozzle on the surface heating of an Apollo capsule and noted the same tendency of the flow field to have separate flow regimes that are dependent on the thrust magnitude [4].

For multiple nozzle configurations, a test with four nozzles in close proximity to the centerline of a flat faced semiellipsoid shape produced results which suggest that for low thrust values in supersonic flow, the pressure on the forebody inboard of the nozzles does not decrease as quickly as it does outboard of the nozzles with increasing thrust. As thrust increases, the pressure is eventually reduced over the entire forebody to a roughly constant value. At low thrusts, jet plumes are distinctly expanding without interaction between the jets. As thrust increases, the plumes coalesce and take on the shape of a single plume [5]. A test on a 60° sphere cone with three nozzles near the periphery of the vehicle showed agreement with these trends. The pressure distribution inboard of the nozzles is relatively undisturbed for low thrusts, while increasing thrust will eventually cause the entire forebody to have pressure reduced to a nearly constant value. This test also

TABLE OF CONTENTS

1. INTRODUCTION.....	1
2. GEOMETRY DESCRIPTION	2
3. METHODOLOGY	3
4. CENTRAL CONFIGURATION ANALYSIS.....	3
5. PERIPHERAL CONFIGURATION ANALYSIS.....	12
6. CONCLUSIONS	20
7. FUTURE WORK.....	21
REFERENCES	21
BIOGRAPHY	22

1. INTRODUCTION

Supersonic retropropulsion (SRP) is a potential enabling technology for entry, descent, and landing (EDL) in environments where traditional deceleration technology may be insufficient. In particular, for EDL in the Martian atmosphere, the use of blunt bodies and supersonic parachutes may not provide the required deceleration as entry mass increases or the trajectory may violate deployment constraints on the systems [1]. Employing retropropulsion at supersonic speeds can replace or augment current supersonic decelerator technology to reach a desired trajectory end state.

¹ 978-1-4244-7351-9/11/\$26.00 ©2011 IEEE

² IEEEAC paper#1190, Version 3, Updated 2011:01:11

shows distinct jets at low thrust conditions with the jets eventually coalescing at higher thrusts [2].

To model SRP, it is prohibitively expensive to run a wind tunnel test for evaluation of a range of candidate architectures and flight conditions. Using computational fluid dynamics (CFD) will allow for a wide range of configurations and conditions to be analyzed and used in the design of future SRP systems. However, the complex flow fields created by an underexpanded jet interacting with a bow shock create a scenario which is potentially difficult to model due to an increased sensitivity to CFD modeling choices and grid properties. The various wind tunnel results provide anchor points for verification of CFD solutions to determine the ability of a computational tool to model SRP. As part of the analysis of the single nozzle on an Apollo capsule, CFD was performed at various flow conditions to predict the interactions of the SRP flow field, and show good agreement with expected results [4]. More recently, preliminary investigations into other geometries have also been performed using a variety of CFD tools. These investigations concentrated on a few flow conditions for each configuration and compared the CFD results with the available wind tunnel data [6],[7].

This paper will expand on the results for the 60° sphere cone geometry [2] and run a sweep of thrust values for both the central and peripheral configurations. The sweeps will match all available wind tunnel data points to attempt to capture both types of flow regimes, as well as cover intermediary thrust values to determine the continuity of the trends in flow field structure and forebody pressure. The sweeps will also evaluate the ability of a single grid without any grid adaptation to encompass a wide range of thrust conditions and regimes for supersonic retro propulsion.

2. GEOMETRY DESCRIPTION

Two geometries are investigated, consistent with the 60° sphere cone models from the wind tunnel experiments described previously [2]. The central configuration has a single nozzle located along the body axis, and the peripheral configuration has three nozzles located off the body axis. Each model has a 4" base diameter. The nozzles on both configurations are directed axially and are flush with the vehicle forebody, creating scarfed nozzles on the peripheral configuration.

Central Configuration

The single nozzle geometry is shown in Figure 1. The nozzle for this configuration is a 15° conical nozzle with an exit diameter of 0.5". The area ratio for this nozzle is 13.95, as specified in the original wind tunnel report [2]. A truncated sting with the dimensions shown in Figure 1 has been added to the back of the vehicle to simulate the presence of the sting during the actual wind tunnel test.

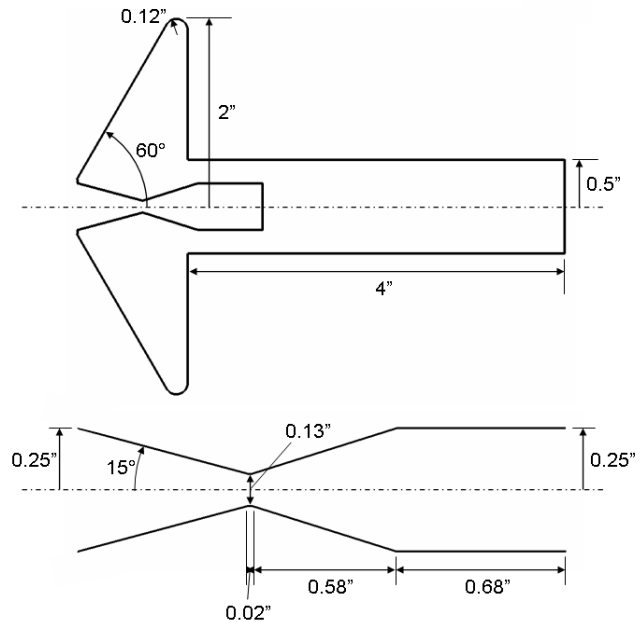


Figure 1: Dimensions for Central Configuration

Peripheral Configuration

The three nozzle geometry is shown in Figure 2 as a slice through the axis of one nozzle. The nozzles are uniformly spaced around the vehicle at 120° increments, and the nozzle center lines are radially located 80% of the base radius from the body axis. Each nozzle is a 15° conical nozzle which has been scarfed such that the exit is flush with the forebody. In the original wind tunnel experiments, the nozzles shared a common feed system, with the individual nozzle housings exposed to the flow [2]. To simplify the CFD model, a cylindrical housing encompasses the entire region behind the vehicle, including each nozzle plenum. The jet total pressure is specified separately for each nozzle.

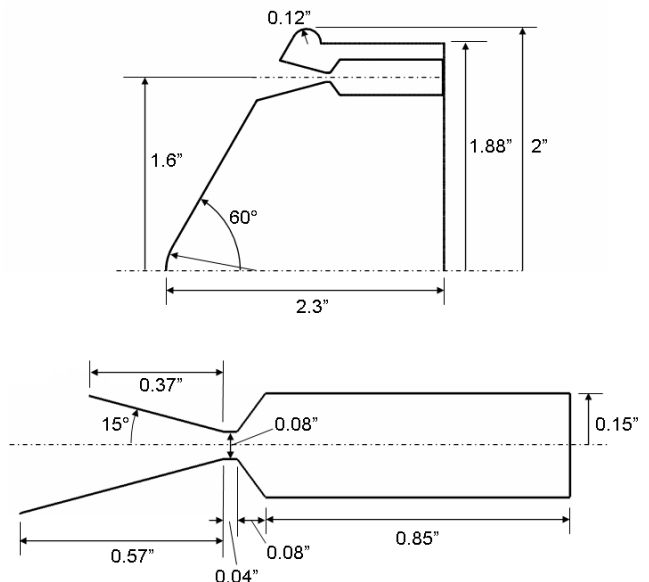


Figure 2: Dimensions for Peripheral Configuration

3. METHODOLOGY

The CFD solutions presented here are generated using FUN3D, a computational tool developed by NASA. For each configuration, the thrust coefficient is varied and the resulting flow field and surface quantities are analyzed. An understanding of the flow field structure, including the locations of the jet terminal shock, stagnation point, and bow shock, is obtained from the flow solution within the computational volume. When possible, these locations are compared to the wind tunnel results to anchor the ability of FUN3D with the current set of input parameters to produce the expected flow structure. Additionally, the CFD solution is checked qualitatively against what is generally expected for underexpanded jet formation. While available schlieren imagery is limited for these cases, a notional understanding of the flow structure can verify whether the computational solution is capturing the relevant flow physics. Surface quantities provide information on pressure distributions and integrated drag for comparison with reported data.

CFD Methodology

FUN3D is a fully unstructured, 3-dimensional flow solver capable of solving the Euler and Reynolds averaged Navier-Stokes equations. The solver can calculate flows for both compressible and incompressible perfect gas assumptions, as well as both thermochemical equilibrium and non-equilibrium. The solver employs a second order, node based finite volume discretization with implicit time stepping. A variety of upwind flux functions, limiters, and turbulence models are available. The solutions shown here are calculated using the calorically perfect compressible equations with local time stepping. All solutions are calculated using the LDFSS flux function with the van Albada limiter and the Menter-SST turbulence model, as used for previous SRP simulations [6],[7].

Flow Conditions

The freestream flow conditions are taken from the wind tunnel data for both configurations. All solutions are run at 0° angle of attack with a freestream Mach number of 2 and freestream stagnation pressure of 2 psi (13.8 kPa). Freestream temperature is not specified in the report, so it is set to 173.4 K, consistent with previous CFD efforts for this geometry. The plenum flow conditions for each nozzle are specified by applying a total temperature and total pressure boundary condition at the inflow boundary of each nozzle. FUN3D enforces subsonic flow normal to the inlet and requires the ratios of total jet pressure to freestream static pressure and total jet temperature to freestream static temperature. The data in the wind tunnel experiment is reported for each case in terms of thrust coefficient (C_T) as defined in Equation 1.

$$C_T = \frac{T}{q_\infty A_{base}} \quad (1)$$

Isentropic relations can be used to back out the required jet stagnation pressure for a given C_T value. For the peripheral configuration, C_T represents the total thrust from all three nozzles. No jet temperature is reported for any case, so jet temperature has been set to 294 K for all cases resulting in an input total temperature ratio of 1.695, consistent with prior computational efforts on this model [6],[7]. The pressure ratios input into FUN3D for both the central and peripheral configuration are reported in Table I. A case with no jet flow is also run for both configurations.

Table I: FUN3D Total Pressure Ratios of Jet on Cases for Central and Peripheral Configurations

C_T	Central $P_{t,jet}/P_\infty$	C_T	Peripheral $P_{t,jet}/P_\infty$
0.47	712.4	1.0	1504.0
0.75	1131.8	1.7	2556.9
1.05	1581.2	3.0	4512.1
2.00	3004.3	4.0	6166.5
3.00	4502.3	5.0	7520.2
4.04	6060.2	6.0	9024.3
5.00	7498.3	7.0	10678.7
6.00	8996.3	8.0	12032.3
7.00	10494.2	9.0	13536.4
8.00	11992.2	10.0	15040.4
9.00	13490.2		
10.00	14988.2		

Grid Methodology

Two different grid generation processes have been used to generate the grids for solutions shown here. No claim is being made about which type of grid generation program is preferred, as the choice of different software was driven by resource availability. For the preliminary grids presented for both configurations, the grid generation process used GridTool and VGrid to generate a fully tetrahedral mesh with anisotropic cells in the boundary layer. The grids used for the primary C_T sweeps are generated using Gridgen v15.15, which allows for mixed cell type grids.

4. CENTRAL CONFIGURATION ANALYSIS

A single nozzle located along the body centerline creates a flow field where an underexpanded jet plume exhausts from the nozzle and interacts with the bow shock present in supersonic flows [6]. The boundary of the jet plume is driven by a shear layer between the jet flow and recirculation regions that form outboard of the nozzle exit. The plume terminates in a Mach disk to decelerate the jet flow such that a stagnation point forms between the jet terminal shock and the bow shock. The bow shock, which decelerates the oncoming freestream flow, becomes offset

from the body due to the presence of the jet plume. The pressure along the forebody surface drops when the bow shock is offset from the vehicle. A schematic of the central configuration flow field is shown in Figure 3, highlighting the flow features of interest for this configuration [6].

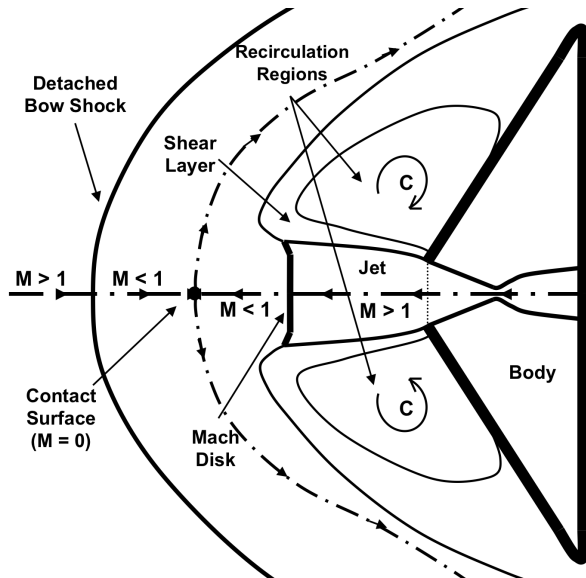


Figure 3: Notional Steady SRP Flow Field Structure for the Central Configuration [6]

From information provided in the original wind tunnel report for this geometry, this flow structure is expected for C_T values greater than approximately 1.05 and should be a steady structure. The wind tunnel report refers to this type of flow field as blunt flow interaction (BFI). For the lower C_T values, a jet penetration mode is reported where the jet terminal shock does not form. Instead, the jet creates an unsteady flow field with no discernable terminal shock and a bow shock far offset from the body. A notional diagram of this flow structure is shown in the wind tunnel report, and shown in Figure 4 as a reference for the CFD solutions at relevant thrust levels [2]. This type of flow field is referred to in the report as long jet penetration (LJP). CFD solutions are generated for C_T values covering both flow structures.

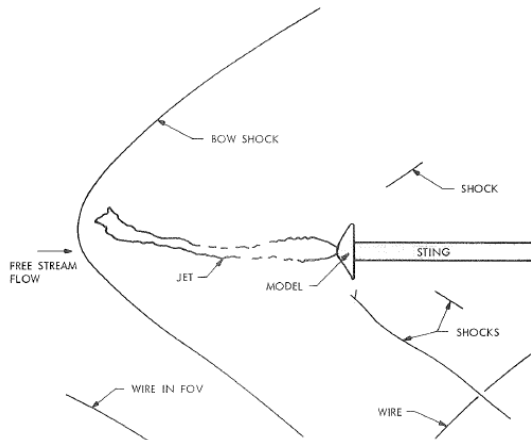


Figure 4: Notional SRP Jet Penetration Flow Structure for the Central Configuration [2]

Preliminary CFD Solutions

The preliminary investigation was performed before the recent CFD efforts [6], [7] had been made, so there was little understanding of the grid requirements to generate a reasonable solution. The primary features of interest were expected to be forward of the vehicle, so the initial grids have the exit plane located at the shoulder of the vehicle. While these solutions do not agree with experimental results as well as is desired, the CFD simulations do provide insight into requirements of the computational domain for modeling supersonic retropropulsion. The grids used in this study are generated using the NASA developed grid generation tools Gridtool and VGrid, where the grid resolution can be uniformly altered by setting scaling parameters in the grid generation process. These scaling parameters were used to create four levels of resolution within the same computational boundaries to gauge the effects of grid resolution on SRP flow fields. The study focused on C_T values that have available experimental data for comparison. The four grid resolutions used in this investigation are detailed in Table II.

Table II: Preliminary Central Configuration Grids with Thrust Conditions Run on Each

Grid	Number of Nodes	C_T Values Run
1 (coarse)	0.30e6	0.47, 0.75, 1.05, 1.50, 2.00, 4.04, 5.50, 7.00
2	0.40e6	0.75, 1.05, 2.00, 4.04
3	0.55e6	0.75, 1.05, 2.00, 4.04
4 (fine)	1.63e6	1.05, 4.04

Flow Structure—The flow field structures are shown for the common C_T values of 1.05 and 4.04 in Figure 5 and Figure 6 respectively for the coarsest and finest grids. The $C_T = 1.05$ solutions show no clearly defined jet terminal shock for either grid resolution. This is not necessarily unexpected, as this thrust coefficient is noted in the wind tunnel results as being at or near the transition between the jet penetration mode and the steady flow structure characterized with a jet terminal shock. Both types of flow are reported for this C_T value in the wind tunnel results, indicating that having conditions that are slightly off in either direction may provide drastically different solutions if the grid is sufficient for capturing both types of flow fields. Neither type of flow interaction is definitively seen, indicating that these levels of grid resolution are not sufficient to capture the flow interaction at low thrust values. The higher resolution grid 4 does show a longer jet plume, which would indicate that the solution is tending towards a jet penetration mode. The bow shock is smoother in grid 4 due to the finer cell resolution for that grid.

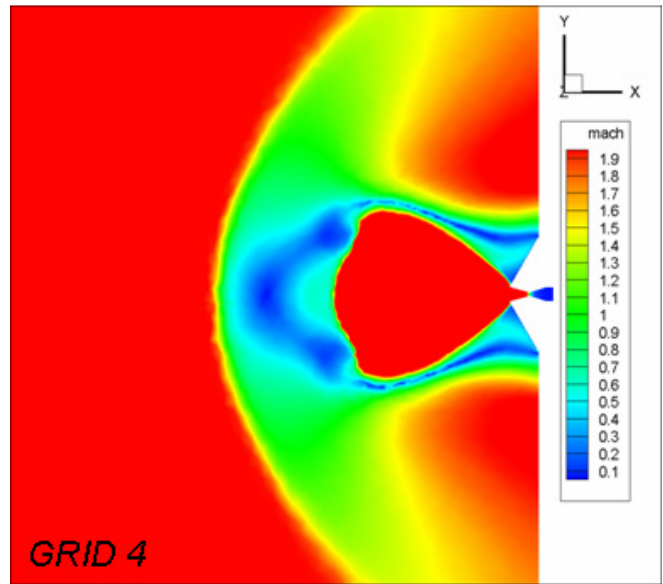
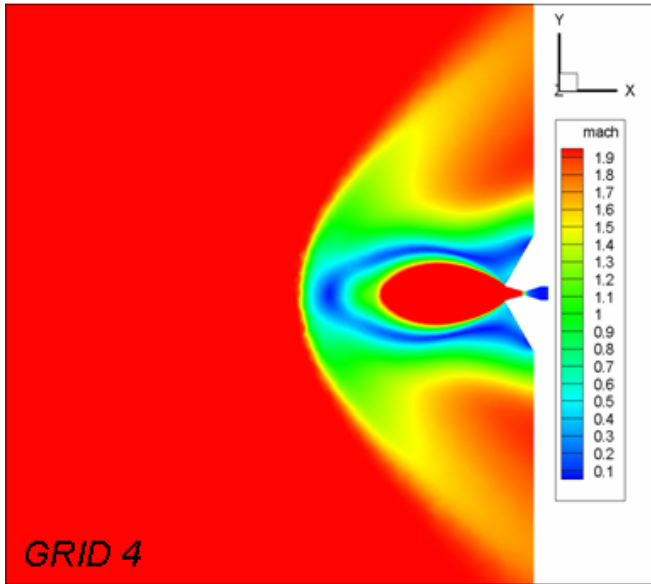
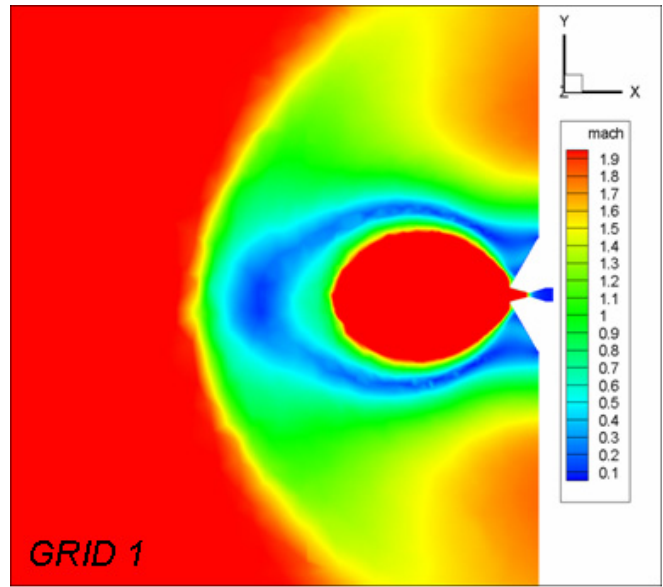
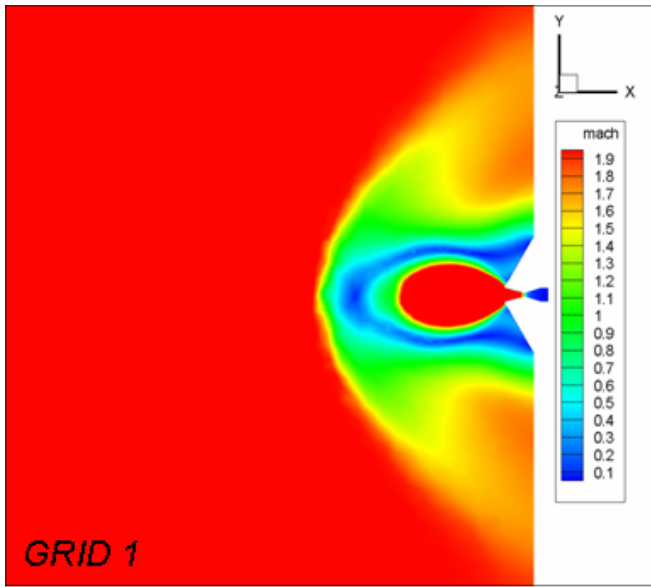


Figure 5: $C_T = 1.05$, Mach Contours for Preliminary Flow Structure Comparison

Figure 6: $C_T = 4.04$, Mach Contours for Preliminary Flow Structure Comparison

The $C_T = 4.04$ solutions only show a jet terminal shock for the finest grid. The three lower grid resolutions all show a flow structure similar to that shown for grid 1, where the jet boundary does not fully form. This prevents the triple point and Mach disk from forming at the termination of the jet plume, as seen in Figure 6. For the finest resolution seen in grid 4, the jet terminal shock forms at the termination of the jet plume. This is a stronger indication than seen in the lower C_T value that grid resolution is a significant driver towards the accuracy of the flow field. Grid resolution does not only control the smoothness of the flow features, but also the shape of the flow features. A low grid resolution may not provide an adequate solution for preliminary analysis of SRP geometries because the plume structure may have a completely different shape than is expected due to the coarseness of the grid.

The jet terminal shock locations are shown in Figure 7 for all four grids. Each distance is normalized by the body diameter and measured from the nozzle exit. For the solutions where no Mach disk forms clearly, this location is the axial distance where the jet flow transitions from supersonic to subsonic flow. For all thrust coefficients, the three coarsest grid resolutions show a consistent plume shape whose size varies as thrust increases. None of these solutions show a terminal shock for $C_T > 1.05$, and none show any jet penetration at low C_T values. These grids do not have sufficient resolution in the plume region to capture the primary flow features. For grid 4, a terminal shock does form for higher C_T values. This creates a Mach disk location closer to agreement with experimental results, though there is still an overprediction. The plume appears to expand further outboard than is indicated in the available schlieren images, which could affect the terminal shock location.

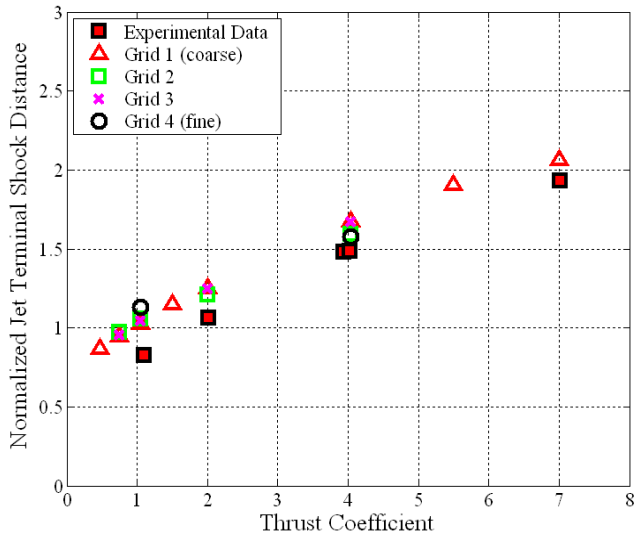


Figure 7: Normalized Jet Shock Location for Preliminary Grid Comparison

The stagnation point standoff distances are shown in Figure 8. The stagnation point locations do not necessarily provide good feedback on the adequacy of the grid to capturing the flow physics because the comparison to the wind tunnel results is skewed. There is no clear method reported for how the stagnation point location is determined from the schlieren image for a given flow. The shocks show up clearly in the schlieren images, but the stagnation point is not as obvious. In the CFD solution, the stagnation point is found using streamlines in the jet plume and freestream flow and locating the convergence point of the streamlines. All grids are in agreement with each other for the stagnation point location, and all show consistent overprediction when compared to the wind tunnel data. Grid 4 shows more jet penetration at $C_T = 1.05$ so the stagnation point for this case is also located further from the nozzle exit plane.

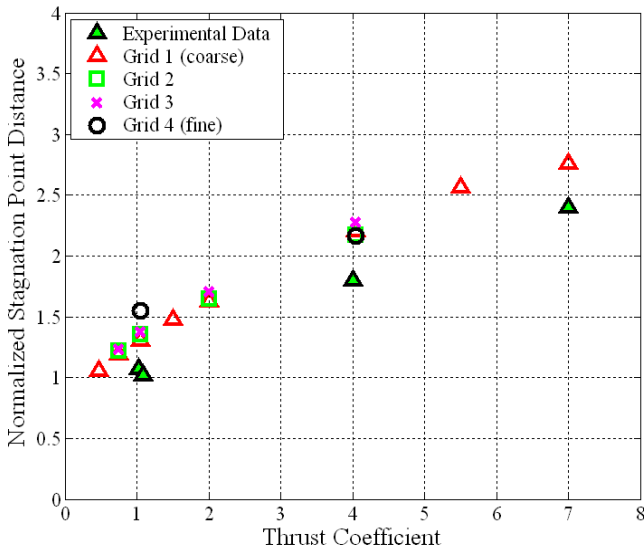


Figure 8: Normalized Stagnation Point Location for Preliminary Grid Comparison

The bow shock standoff distances are shown in Figure 9. As with the jet terminal shock and stagnation point, the solutions show a consistent overprediction of the bow shock locations for the steady jet plume at higher C_T values. For the low thrust coefficients, since no jet penetration is seen in any of the CFD solutions, the bow shock is not located far from nozzle exit as is reported in the wind tunnel results. Thus there is a drastic underprediction of the bow shock location at C_T values less than 1.05. Grid 4, with a Mach disk formed, does show better agreement at $C_T = 4.04$, which further confirms that correctly capturing the jet plume shape is important for determining all aspects of the SRP flow field. At $C_T = 1.05$, the bow shock is located further from the body than in the coarser grids, which is again caused by the increased jet penetration seen in the solution.

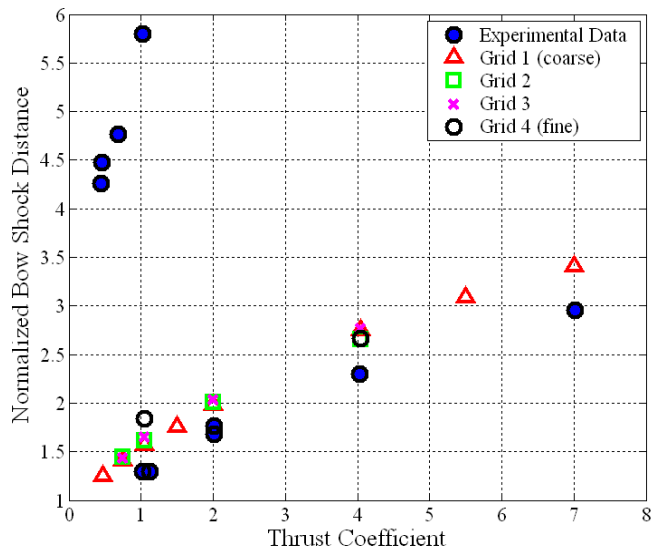


Figure 9: Normalized Bow Shock Location for Preliminary Grid Comparison

Aerodynamics—The pressure distribution on the body varies with thrust coefficient due to the changing size and expansion of the jet plume. The trend seen in the wind tunnel results for the central configuration shows that the pressure along the forebody decreases as thrust coefficient increases. As the jet plume expands, the diameter of the plume increases and the bow shock is offset further from the vehicle. As the thrust coefficient increases to $C_T = 4.04$ and higher, the pressure along the forebody becomes nearly constant as the vehicle is immersed in a wake type flow. There is a significant pressure rise in the region near the jet caused by the jet expansion out of the nozzle exit. The pressure distributions for Grid 1 are shown in Figure 10 and Figure 11 for all thrust coefficients tested. They show the decrease in pressure expected as C_T increases as well as the pressure rise near the jet.

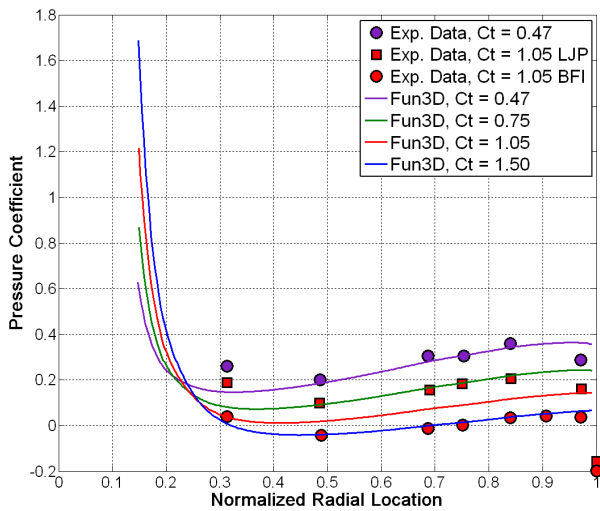


Figure 10: C_p Distribution Comparison for Low C_T Values on Preliminary Grid 4

Of particular note is the $C_T = 1.05$ solution, which shows a pressure distribution between that reported for the jet penetration and steady flow modes. Since the CFD solution does not clearly show either mode, the pressure distribution also does not clearly agree with either mode. Instead, some intermediate type of flow structure is formed in the CFD simulation. For the higher thrust coefficients shown in Figure 10, the pressure drops to a nearly constant value as C_T increases. There is still a slight variation with C_T , but the change is less than at low thrust coefficients.

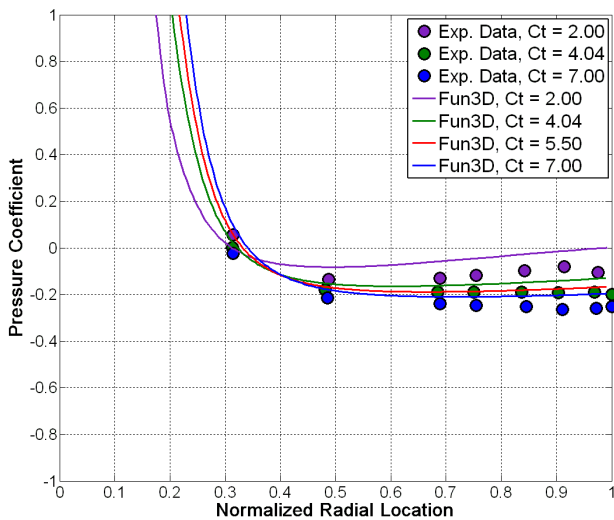


Figure 11: C_p Distribution Comparison for High C_T Values on Preliminary Grid 4

For all grids, the integrated drag coefficient (C_D) is shown in Figure 12. This encompasses any changes in pressure distribution with changing grid resolution because a lower pressure on the vehicle will cause a lower integrated drag coefficient. Note that for comparison with the wind tunnel results, this drag coefficient does not include the pressure along the aft portion of the vehicle; it is only an integration

of the pressure along the forebody and shoulder. The wind tunnel test did not record the drag coefficient directly, but integrated the pressure port data to determine each C_D value. This could cause some discrepancies in the comparison, as the wind tunnel distributions may not fully cover the changing pressure across the entire forebody. For $C_T = 4.04$, increasing the grid resolution shows better agreement in the integrated drag coefficient. As the plume expansion becomes more in line with expectations, the pressure along the forebody also agrees better with expectations. For the lower thrust coefficients, the agreement is not as good due to the CFD simulations not correctly determining the jet penetration that is expected at those C_T values. However, even with the inaccurate plume shapes, the pressure along the forebody is still increased at lower C_T values.

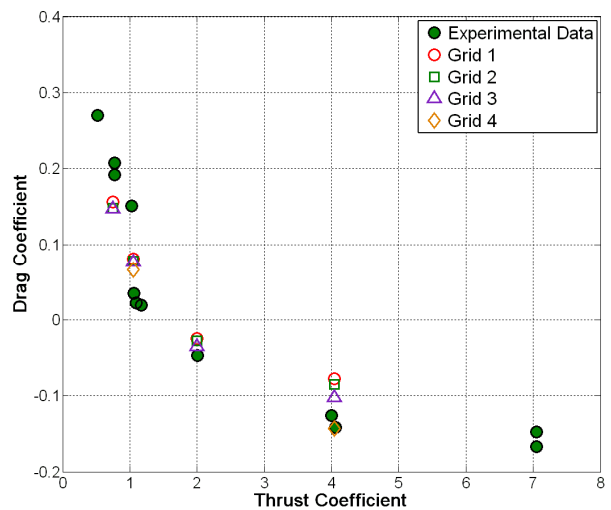


Figure 12: C_D Comparison for Preliminary Grids

Solution Issues—These solutions provide significant information about some grid properties that should be considered when investigating supersonic retropropulsion. First, increasing the grid resolution creates a flow field that provides a closer match with the expected plume shape. If the grid resolution is too coarse, then the flow field shape will not be modeled correctly. This creates a flow field with elongated jet plumes and increased standoff distances for flow features. This also causes errors in the pressure distribution and integrated drag on the vehicle forebody.

Second, placing the exit plane at the shoulder of the vehicle causes two main issues when running the flow solver. Since the default Riemann boundary condition for farfield flow is not applicable, a shock forms at the exit plane as the solver tries to resolve the boundary condition. The effects of the shock feed back to the jet plume, significantly altering the plume structure. An example of this is shown in Figure 13 for $C_T = 1.05$. While the jet does appear to show the penetration mode, it is not doing so because of the actual physics of the problem, but rather the effect of a non-physical artifact in the flow from the boundary condition.

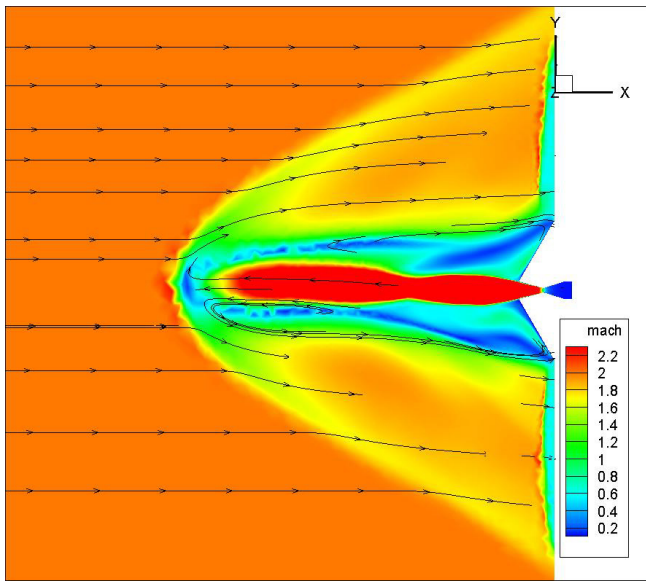


Figure 13: Preliminary Grid Exit Plane Issue

The fix to the exit plane issue for this grid is to set the exit plane to an extrapolation condition. This introduces the second issue, which is that the flow solver can not converge on a solution using second order spatial differencing for these grids. Inevitably, instabilities occur in the flow, causing the solution to diverge and end the simulation. Thus, all of the solutions shown previously are the result of first order spatial differencing with the extrapolation boundary condition.

Higher Resolution CFD Solutions

Taking into account the grid effects seen in the preliminary investigation, a new grid has been developed to improve the CFD simulations on the central configuration. The exit plane has been placed far aft of the vehicle (~10 body diameters) to allow the subsonic wake region to form. This prevents any potential boundary condition issues from impacting the SRP flow field. Also, the grid resolution in the jet plume region has been significantly increased to better capture the plume structure and improve the solutions for varying C_T . This grid is created with Gridgen V15.15 and has a mix of hexahedral cells in the nozzle and boundary layer and tetrahedral cells in the freestream. While the finest grid from the preliminary investigation had 1.63 million nodes, this grid has 19.78 million. Some of the increase in number of nodes is attributed to the increase in the volume of the computational domain, but the primary cause for the increase is the reduction in cell size in the jet plume region. The cases run on this grid follow the information given in Table I for the central configuration. All of these solutions have been run with second order spatial differencing, as the errors that caused the preliminary solutions to diverge have been corrected.

Flow Structure—For C_T values less than 1.05, the beginnings of a jet penetration mode are seen in the flow structures, as shown in Figure 14. The grid resolution does

not appear to be fine enough to fully capture the jet penetration flow structure, but it is sufficient to show more penetration than the preliminary grids. As the thrust coefficient increases, the length of the jet increases and the bow shock standoff distance increases, consistent with the wind tunnel results. It appears that a second plume cell is in the process of forming at the end of the jet plume for each solution, which would push the bow shock further off the body. It is possible that this second cell does not fully form due to dissipation in the simulation.

For C_T values greater than 1.05, the flow fields clearly show the expected jet plume shape where the plume expands out of the nozzle and terminates in a Mach disk. A sampling of these solutions is shown in Figure 15. Note that a different Mach contour scale is used for these images as opposed to Figure 14 to better show the flow features at each C_T value. As C_T increases, the jet expands to a larger diameter and the Mach disk forms further from the body. Unlike the solutions on the preliminary grids, the plume is narrow as it expands out of the nozzle. The coarse grids from the preliminary investigation show a round jet boundary, as the grid is too coarse to properly resolve the shear layer along the jet boundary. Even the finest preliminary grid shows a significant expansion outboard of the vehicle axis, as seen in Figure 6. While the jet is not rounded in the solution from preliminary grid 4, it also does not have the smooth transition seen in the higher resolution grid. Instead, it is a very linear expansion with a sudden transition at the Mach disk. Each jet for the higher resolution grid shows a smooth transition along the jet boundary from the nozzle exit to the termination shock.

Though the extent of plume expansion varies drastically from the low thrust to high thrust conditions, the shape remains the same for the steady flow field. Providing sufficient cell size to resolve the largest expected plume will also allow the grid to adequately solve lower thrust conditions. If a jet penetration mode is expected, then the grid resolution that works for high C_T values may not sufficiently capture all of the jet penetration. In this case, there are signs that jet penetration may be occurring, so further refinement of the grid may be necessary to attempt to capture the jet penetration to a higher degree.

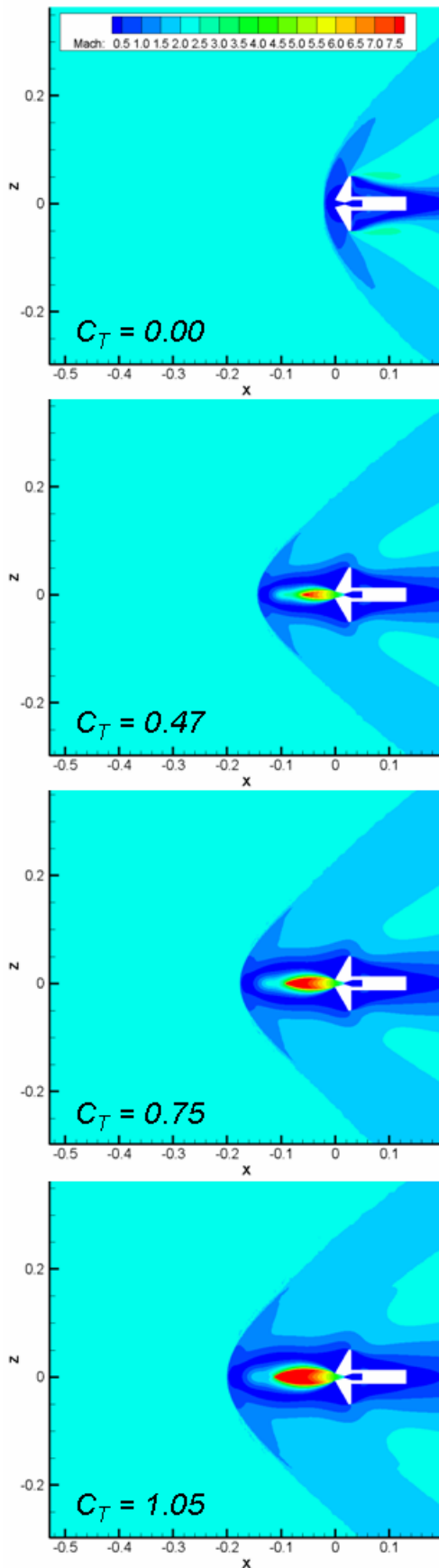


Figure 14: Low C_T Flow Field Structures Showing the Beginnings of the Jet Penetration Mode

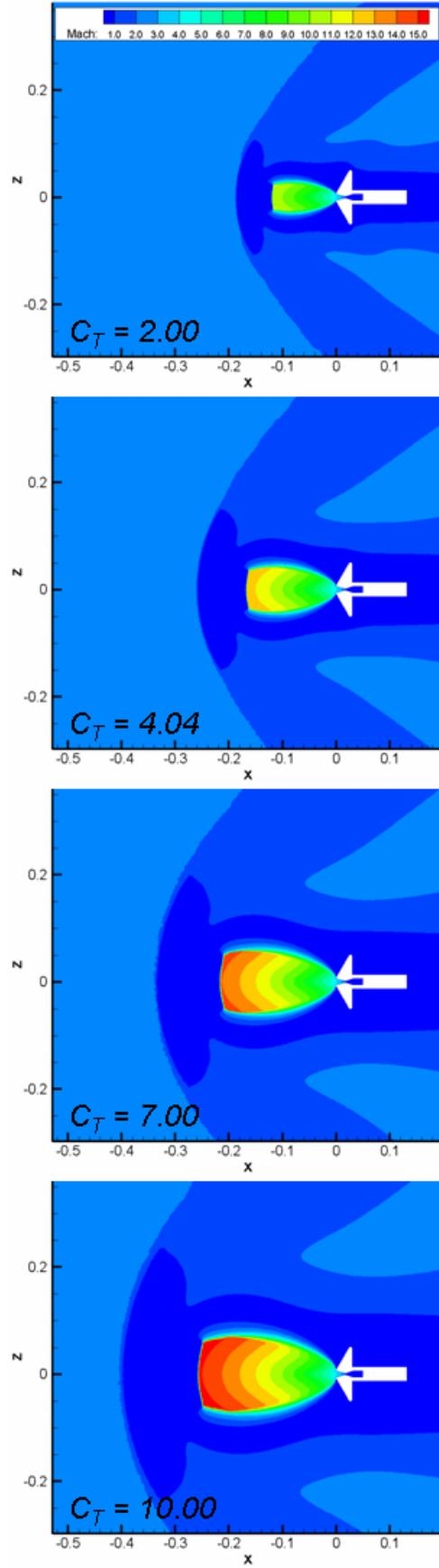


Figure 15: High C_T Flow Field Structures Showing the Steady Plume Shape with a Mach Disk

As with the preliminary grids, the distance from the nozzle exit for the primary flow features can be taken from the CFD simulations and compared to the available wind tunnel data. The bow shock, stagnation point, and jet terminal shock locations for the cases run on the high resolution grid are shown in Figure 16. Note that there is still a consistent over-prediction of the flow feature locations for the steady flow structure solutions. It is unclear why this is the case, and if the difference occurs in the CFD simulation, the reported data, or both. It is possible that there is some discrepancy in the actual wind tunnel data because it is unknown if the standoff information is averaged over a run or taken as a snapshot in time. This is particularly relevant for the jet penetration cases, where the flow field is reported to be highly unsteady. Depending on when the measurement of standoff distance is taken, the value may not compare favorably with the CFD simulation. It is also possible that the local time stepping, grid resolution or equation settings, such as flux limiter and turbulence model, result in larger standoff distances for the CFD simulation than should exist.

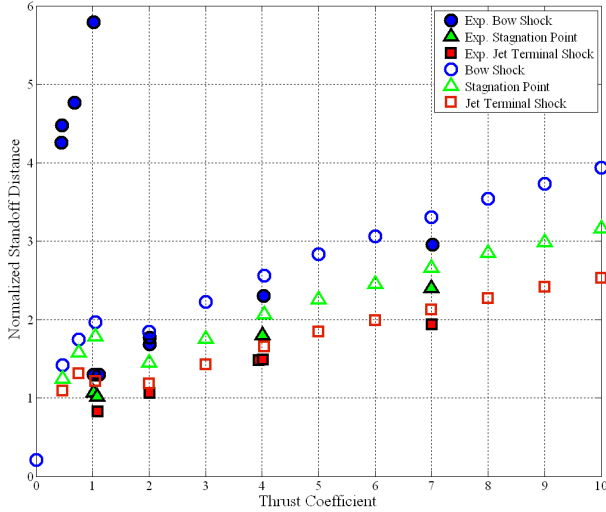


Figure 16: Flow Feature Standoff Distance Comparison for Higher Resolution Grid

A comparison between the standoff distances of primary flow features from Grid 4 and the current high resolution grid is shown in Table III for $C_T = 1.05$ and $C_T = 4.04$. At the higher thrust coefficient, the bow shock and stagnation point are closer to the vehicle for the high resolution grid, which is in better agreement with the experimental data. Since the resolution is higher for the current grid, the widths of the bow shock and stagnation region are better resolved. Though the preliminary investigation shows a lower jet standoff distance, it is difficult to compare these as the jet shape varies drastically between the two solutions. Since the jet boundary determines the location of the Mach disk, significant discrepancies in the boundary shape can result in vastly different terminal shock locations. For the lower thrust coefficient, the high resolution grid shows higher standoff distances for each flow feature. If this C_T should

show jet penetration, then this is better agreement because some penetration is being shown on the high resolution grid and none is seen in the preliminary solution. Since this is the bounding case between the two modes, it is unclear which should be the dominant mode. Further investigation into conditions around this transition C_T would help to show if the sharp transition between the modes can be captured by CFD, or if the computational simulation creates a smoother transition between jet penetration and a terminal shock.

Table III: Standoff Distance Comparison between Preliminary and Higher Resolution Grids

	$C_T = 1.05$		$C_T = 4.04$	
	Grid 4	High Res	Grid 4	High Res
Bow	1.84	1.97	2.66	2.56
Stag.	1.55	1.78	2.17	2.07
Jet	1.13	1.21	1.58	1.65

The current solutions compare favorably with previous computational efforts on the central configuration [6],[7]. The standoff distances for the bow shock, stagnation point, and jet terminal shock are shown in Table IV for $C_T = 7.00$, comparing the current solution with other published solutions generated using DPLR, FUN3D, and OVERFLOW CFD codes. While the previous studies show that each code computes a different overall jet structure at this thrust condition, the axial locations of the flow features agree well between the different solutions, though the locations are not exactly identical. Since each grid is different, this is an indication that even a well refined grid may cause some differences in the solution, but it should be close enough to provide a reasonable simulation of the SRP flow field.

Table IV: Standoff Distance Comparison for $C_T = 7.00$ between Higher Resolution Grid and Previous Efforts

	Bow	Stagnation	Jet
Current	3.3	2.6	2.1
FUN3D [6]	3.0	2.4	1.9
DPLR [7]	3.5	2.8	2.2
FUN3D [7]	3.4	2.8	2.2
OVERFLOW [7]	3.5	2.9	2.2
Experiment	3.0	2.4	1.9

Aerodynamics—As with the preliminary grids, the pressure variation with changing thrust coefficient follows the expected trend. As thrust coefficient increases, the pressure along the vehicle decreases. The pressure distributions for C_T values of 0.00, 0.47, and 1.05 are shown in Figure 17. The jet off condition shows a slightly higher pressure coefficient along the forebody, but in general it agrees well with the experimental data points. There is a kink in the C_p

curve near the nozzle exit which appears to be caused by the flow interaction with the open nozzle. For the other C_T values, the pressure distribution is significantly lower than expected. Just looking at the pressure distribution for $C_T = 1.05$ would indicate that the flow field resembles more of the steady flow with a jet terminal shock, which disagrees with the results seen visually in Figure 14. It could be that since the full jet penetration is not being resolved, the pressure is following the steady distribution. The preliminary grid 4 pressure distributions shown in Figure 10 have more consistent agreement across the forebody for these thrust coefficients. Since the preliminary simulation shows no hint of the jet penetration, it is clear that the shape and mode of the jet plume has a large effect on the pressure distribution of the forebody.

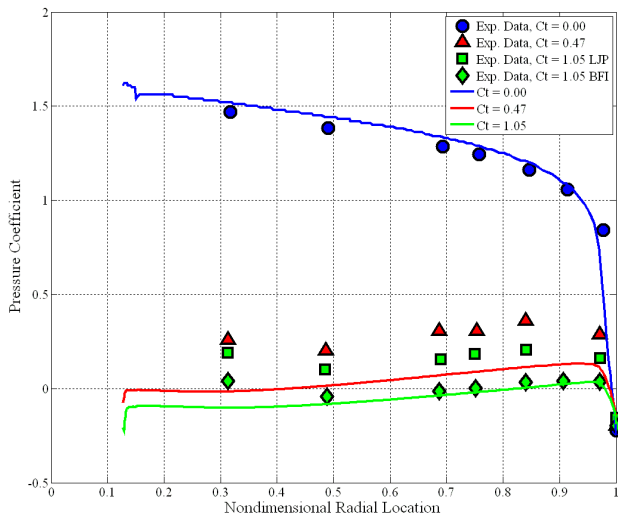


Figure 17: C_p Distribution Comparisons for Low C_T Conditions on Higher Resolution Grid

For the higher thrust coefficients with a steady flow field, the pressure distributions for C_T values of 2.00, 4.04, and 7.00 are shown in Figure 18. There is better agreement with experimental results for these conditions as opposed to the lower thrust coefficients, indicating that the steady flow solutions are closer to the expected flow fields. Of note though is that the pressure rises near the nozzle do not match up with the experimental data points. For the preliminary grid 4, the pressure distribution agreed reasonably well with the first experimental data point, while the agreement along the forebody was worse. Since the jet plumes have significantly different expansion shapes for $C_T = 4.04$, the divergence angle of the flow has a significant effect on the forebody pressure near the nozzle exit. The increased grid resolution and extension of the domain aft of the vehicle appear to have aided in the establishment of the pressure away from the nozzle, as the distribution shape is in better agreement with the experimental data.

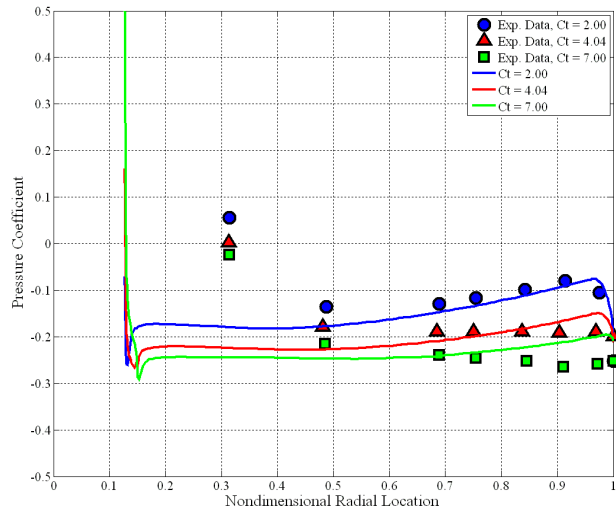


Figure 18: C_p Distribution Comparisons for High C_T Conditions on Higher Resolution Grid

For all thrust coefficients, the integrated drag coefficient is shown in Figure 19 for the higher resolution grid. Across all thrust coefficients, good agreement is shown with the experimental data points, even with the discrepancies seen in the pressure distributions near the nozzle exit. For the jet penetration cases, C_D is slightly lower than expected, most likely due to the jet penetration mode not fully establishing. This is in better agreement than the preliminary grids which show no jet penetration, further supporting that simulating the correct mode has a noticeable impact on the vehicle aerodynamics. For the steady flow fields, the drag coefficient does not level off as is seen for the preliminary grids. Instead, it continues to decrease slightly with increasing thrust coefficient, and better agreement is shown with the experimental data points. Since the jet terminal shock is being generated for all of these cases, the pressure and integrated drag should show better agreement than the preliminary grids that show an inaccurate flow structure.

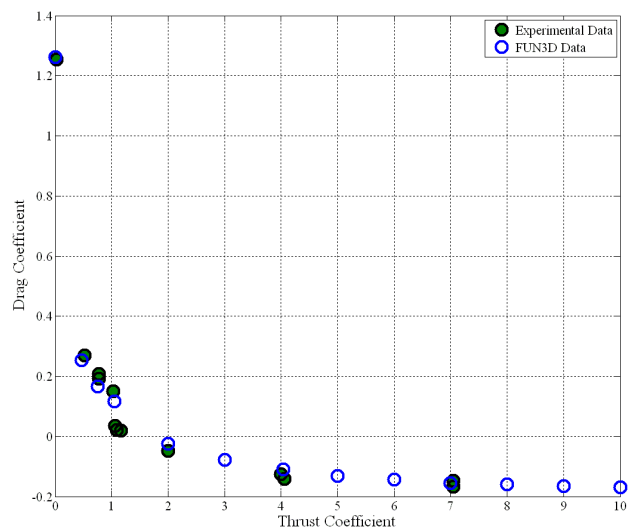


Figure 19: C_D Comparison for Higher Resolution Grid

5. PERIPHERAL CONFIGURATION ANALYSIS

A peripheral configuration creates a much different flow structure from the central configuration. Instead of an axial plume where the jet flow is roughly parallel to the oncoming freestream flow, a peripheral configuration has jets exhausting into a flow which is nominally following the vehicle forebody. This is similar in concept to a jet exhausting into a crossflow, with the additional presence of the bow shock affecting the termination of the jet plume. There is also an added complexity due to the potential for plume interaction depending on the proximity of the nozzle exits and the size of the plumes. The plume shape differs from the axisymmetric plumes seen for the central configuration due to the scarfed nozzle and the jet boundary responding to the turned flow coming through the bow shock, as illustrated in Figure 20 [6]. The jet terminal shock does not resemble the Mach disk seen for the central configuration, but is affected by the altered plume shape. When there is no jet interaction, the stagnation point still forms along the vehicle surface inboard of the jet plumes.

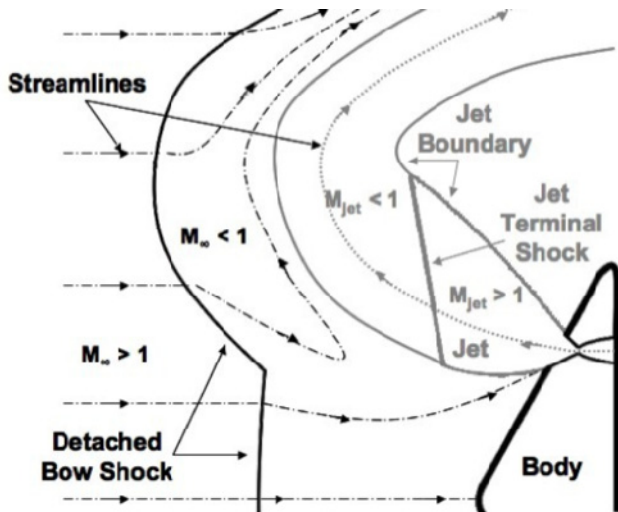


Figure 20: Notional SRP Flow Field Structure for the Peripheral Configuration [6]

From the wind tunnel report, there is no jet penetration mode noted as exists for the central configuration [2]. However, it is noted that the jets interacted with each other at some test conditions. In particular, a total thrust coefficient of $C_T = 4.0$ shows plume interaction and local instabilities in the region between the bow and jet shocks. A significant rise in bow shock standoff distance is reported for $C_T = 5.5$, with a drop then shown at $C_T = 7.0$ [2], indicating that the flow field resulting from plume interaction may be significantly different from the flow field with independent jets. The plume interaction can create a scenario where the flow field resembles that of a central configuration if the jets coalesce into a single plume [6].

Preliminary CFD Solutions

Based on the results from the preliminary central configuration, the initial investigation for the peripheral

configuration includes an examination of the location of the exit plane and its effect on the CFD simulation. This is particularly important for the peripheral configuration because the freestream flow sees a larger effective body due to the presence of the jet plumes. Thus the subsonic wake region aft of the vehicle will require more distance to close. Solutions have been generated on four grids, with the conditions shown in Table V. The x location of the exit plane is measured from the nose of the vehicle. Thus the closest exit plane of 2.5 body diameters is approximately 2 body diameters aft of the back face of the vehicle.

The first three grids in particular are set up to examine the effect of exit plane location on a peripheral configuration CFD solution, so only a limited number of cases are run with target conditions that match available wind tunnel data. Of primary interest are the $C_T = 1.0$ case, which has significant pressure distribution data available, and the $C_T = 7.0$ case, which represents the highest thrust coefficient tested and should provide the largest wake region. The fourth grid is generated based on the results from grids A-C, and fully encompasses the subsonic wake region for all thrust coefficients tested. The sides of the computational domain have also been moved further from the vehicle due to potential boundary interactions seen in grids A-C.

Table V: Preliminary Peripheral Configuration Grids with Thrust Conditions Run on Each

Grid	Exit Plane Location	Number of Nodes ($\times 10^6$)	C_T Values Run
A	2.5D	0.58	0.0, 1.0, 7.0
B	5D	1.00	0.0, 1.0, 1.7, 7.0
C	7.5D	1.17	1.0, 1.7, 7.0
D	20D	2.97	1.0, 1.7, 2.4, 3.0, 3.6, 4.1, 4.8, 5.5, 6.3, 7.0, 8.0, 9.0, 10.0

These grids are generated using Gridtool and VGrid. For grids A-C, the grid sources are kept identical between the grids; however, due to the nature of this grid generation process, the cell structure forward of the vehicle is not identical between the three grids. For the fourth grid, the sources which control grid resolution in the plume region were altered to provide more nodes in the jet region than in grids A-C, as there were concerns about the resolution and its effect on the flow structures seen in grids A-C. The higher thrust coefficient solutions show more variation, and this could be a result of differences in the grids that result from the grid generation process and altered sources.

Flow Structure—The flow fields for all four grids at the common test conditions of $C_T = 1.0$ and $C_T = 7.0$ are shown in Figure 21 and Figure 22 respectively. These images represent a slice through the axis of the vehicle and the center of one nozzle.

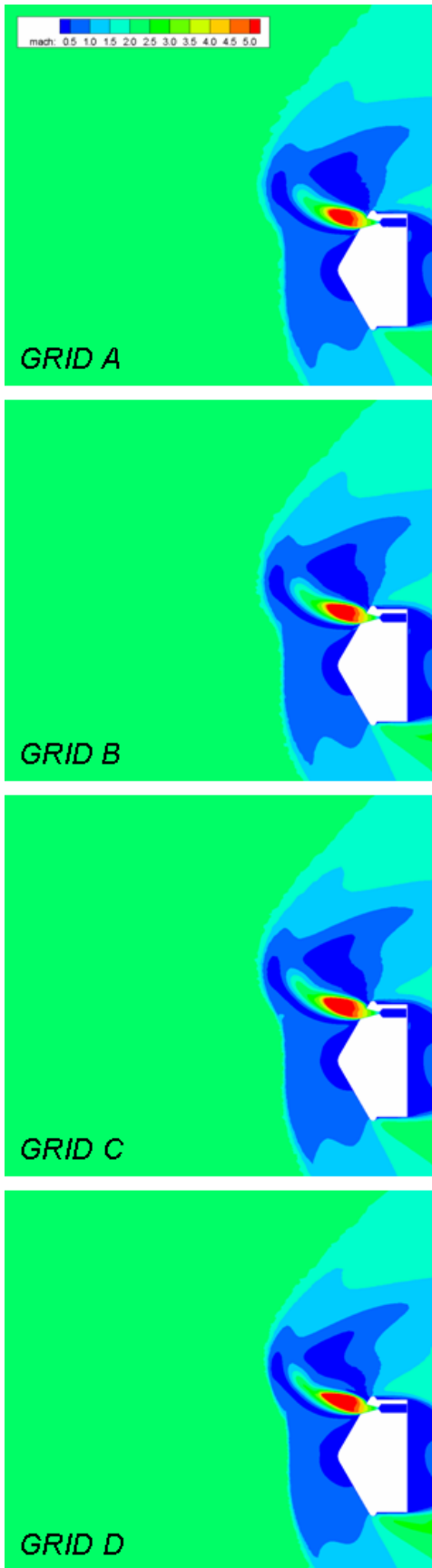


Figure 21: $C_T = 1.0$ Mach Contours for Preliminary Peripheral Configuration Flow Structure Comparison

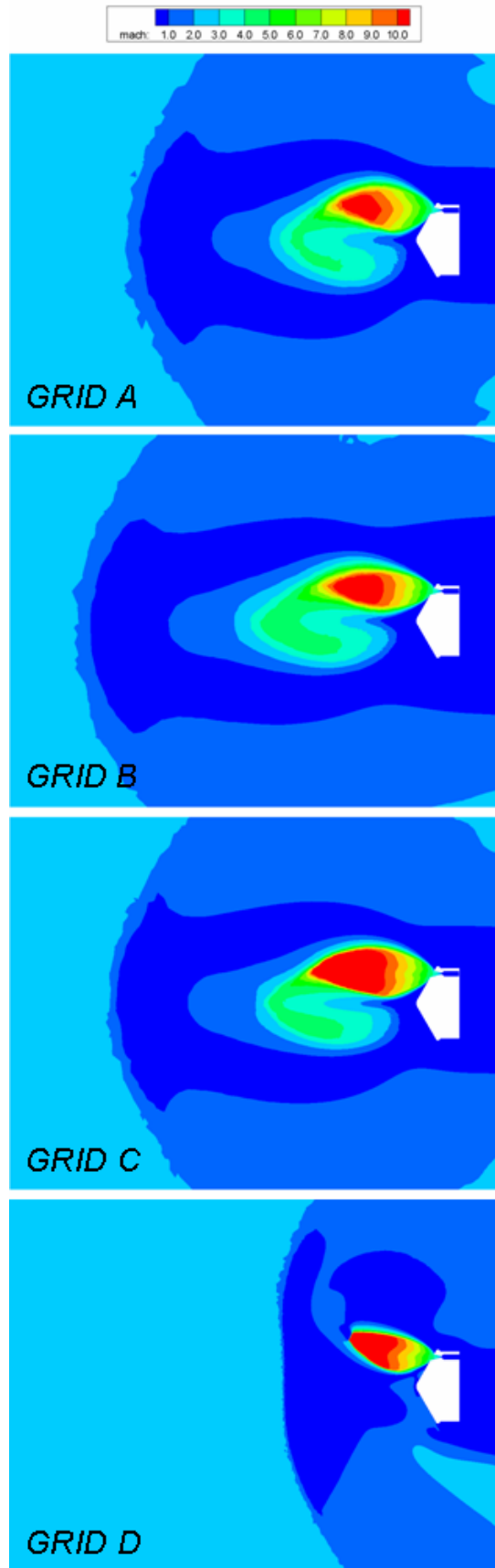


Figure 22: $C_T = 7.0$ Mach Contours for Preliminary Peripheral Configuration Flow Structure Comparison

For $C_T = 1.0$, the solution does not noticeably vary as the exit plane distance from the body is increased. Since these jet plumes have a relatively small expansion, they do not create a large wake behind the vehicle. The exit plane interaction with the wake is negligible, and the flow field forward of the body is unperturbed. The jet plumes do show the expected shape caused by the turned flow along the vehicle forebody. While the jet modifies the shape of the bow shock in the region directly forward of the nozzle, the portion of the bow shock inboard of the nozzles remains undisturbed. This is consistent with schlieren imagery from the wind tunnel data, which shows the three jet plumes independent of each other and the bow shock inboard of the nozzles resembling a normal shock [2]. Grid D, with more focus on the jet plume cell density, shows less blunted contours for the interior of the plume, but the overall bow shock and jet boundary shape are not drastically different.

For $C_T = 7.0$, the solutions vary significantly between each grid. Grids A-C all show significant coalescence between the jet plumes, causing the bow shock to form far forward of the vehicle. Coalescence is seen in the planar slices of Figure 22 as the region where the two jet plumes outside the slice intersect the plane and interact with the visible plume. There is no clearly defined terminal shock for the coalescence structure. The first three grids all show plume expansions prior to coalescence that differ from each other. Grid A shows a wide plume with a thick jet boundary. Grid B shows a narrower plume with the thick jet boundary still present. Grid C shows the wide plume with a thinner jet boundary. Grid B, with its narrower plume structure, has a bow shock located noticeably farther from the vehicle than the other two grids. The thinner plume creates a longer jet, which pushes all flow features farther from the body. It is not clear if the difference in the solutions is a function of the exit plane location only, or a combination of the exit plane and node density discrepancies between the grids. Grid D provides a much different flow structure from any of the other grids. There is no jet coalescence seen in this solution, which causes the bow shock to be much closer to the vehicle. The subsonic wake region for this grid is completely contained within the computational domain, so there should be no boundary condition effects on the plume shape. Additionally, the increased focus on node density in the plume region appears to have resolved the flow field to this current structure. It is unclear from the available data which flow structure is to be expected for this condition. Grids A-C are most likely too coarse to properly resolve the plume shape based on similar resolutions used in the preliminary central configuration grids. Increasing grid resolution should help resolve this discrepancy.

Aerodynamics—As the thrust coefficient increases, the pressure on the body does begin to decrease and a symmetry in the distribution about each nozzle is seen, as shown in Figure 23 for $C_T = 1.0$ and in Figure 24 for $C_T = 7.0$ for all four grids.

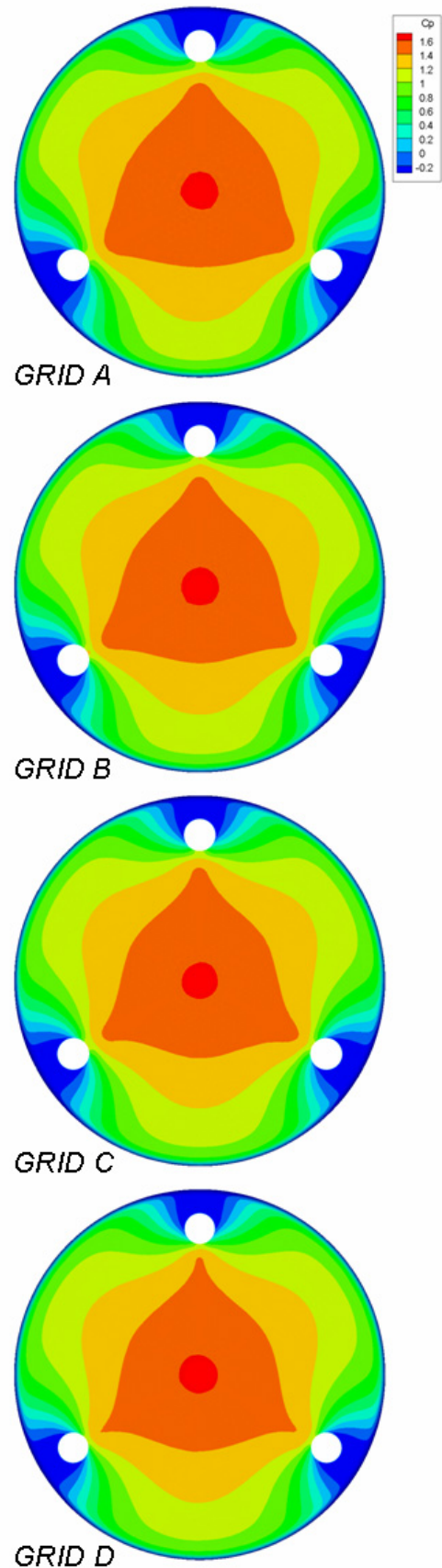


Figure 23: $C_T = 1.0$ C_p Distributions for Preliminary Peripheral Configuration Comparison

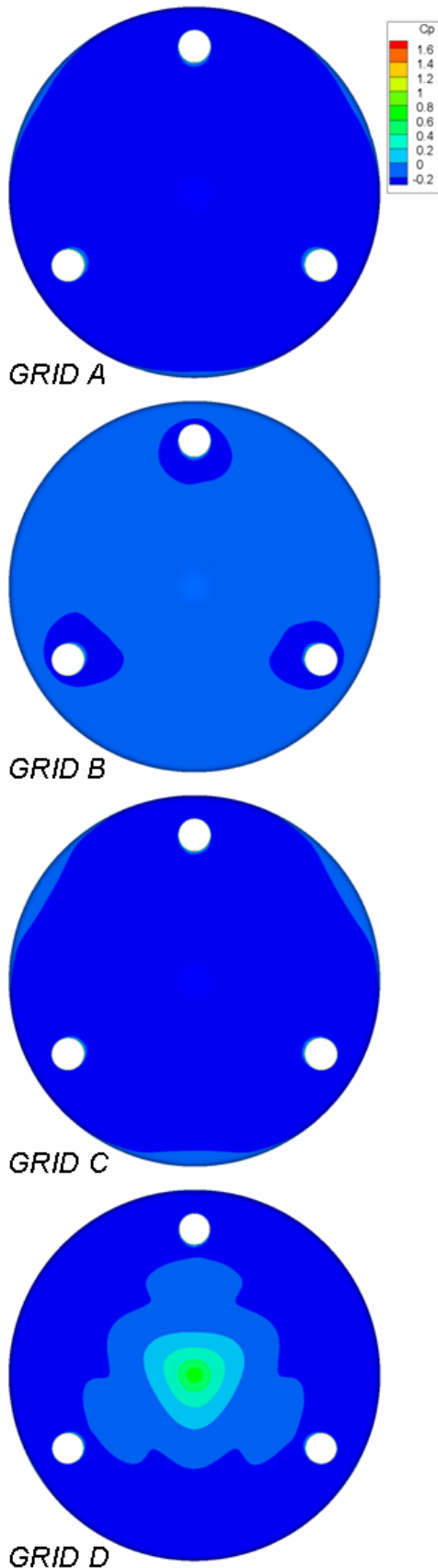


Figure 24: $C_T = 7.0$ C_p Distributions for Preliminary Peripheral Configuration Comparison

Since the flow field for $C_T = 1.0$ is similar for each grid, the pressure solution is not expected to vary significantly between the four grids. Immediately outboard of the nozzle exits, the pressure drops off significantly due to the plume expansion. Inboard of the nozzles, the pressure is still high for this thrust coefficient because the bow shock inboard of the nozzles is undisturbed, preserving aerodynamic drag.

For $C_T = 7.0$, the varied flow structures between the four grids also show a significant effect on the forebody pressure for each solution. Grid A and grid C show similar pressure distributions, where the entire forebody is reduced to a low pressure value, consistent with their similar flow structures. Grid B shows longer, thinner jet plumes and a higher pressure preserved on the forebody. Though the plumes do still coalesce and reduce the pressure on the forebody, it is not to the same level as grids A and C. For grid D with no jet interaction in the flow structure, high pressure remains inboard of the nozzles because the plumes are not fully shielding the forebody. The available data suggests that the pressure should resemble that seen in grids A-C, but uncertainties in the effect of grid resolution on the flow structure and pressure distribution indicate that this agreement may be coincidental.

The integrated drag coefficient trend is shown for all four grids in Figure 25. The agreement between the four grids at $C_T = 1.0$ is confirmed here as well, with all four grids providing very similar drag coefficients. For grid D, as thrust is increased, the drag is consistently overpredicted. Since grid D does not have jet coalescence for any solution, more pressure is preserved inboard of the nozzles and the drag coefficient increases. There may also be a discrepancy from the wind tunnel results, as C_D is integrated from a limited number of pressure ports. These may not cover the full pressure variations, which would affect the final value.

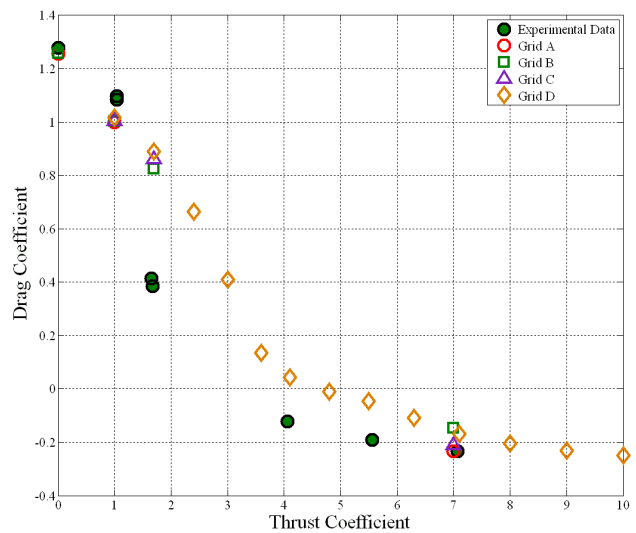


Figure 25: Integrated C_D for Preliminary Peripheral Configuration Comparison

Solution Issues—From this initial investigation into the exit plane location, it is difficult to say with certainty if the exit boundary condition alone significantly affects the flow field forward of the vehicle and the pressure along the surface. Since the cell density also varies between the grids, there may be a coupling of effects from the grid resolution and the exit plane. The $C_T = 1.0$ solutions are shown in Figure 26 for grids A-C. The subsonic regions are clearly visible, and it is apparent that the only intersection between the subsonic wake and the exit plane occurs for grid A. The subsonic wake is important because only flow traveling at subsonic speeds can pass information back to the body and potentially impact the flow solution. The flow fields for all three grids are similar, even with the intersection in grid A; further supporting that the low thrust coefficient solution is independent of the exit plane for the grids tested.

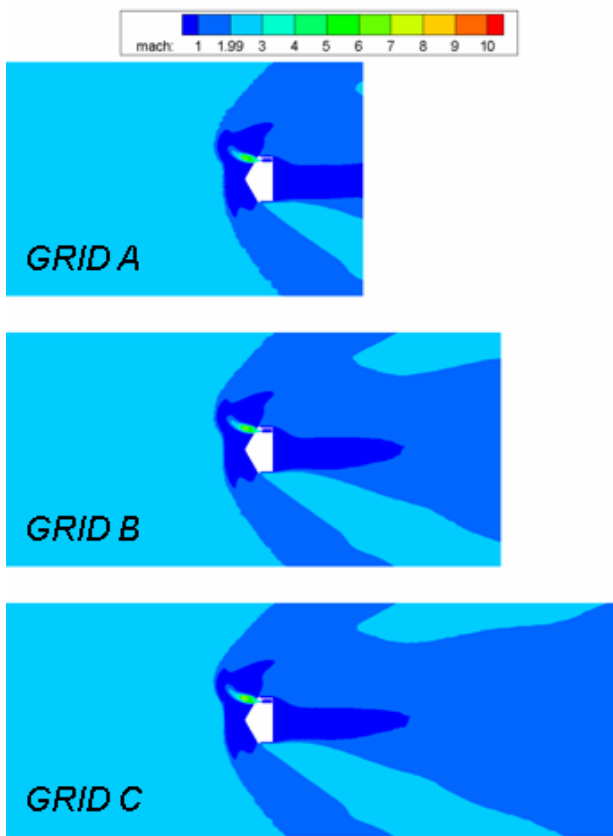


Figure 26: Exit Plane Effects on $C_T = 1.0$ Mach Contours for Peripheral Flow Structure

For $C_T = 7.0$, the exit plane does have an effect on the wake region of the flow field, as shown in Figure 27 for grids A-C. In particular, for grid C, the subsonic wake is expanding at the exit plane, which should not occur. The subsonic wake should close behind the body, creating fully supersonic flow at the exit. For all grids, the subsonic wake intersects the exit plane, and the shape of the subsonic region varies for each solution. This could be impacting the jet boundary, since the subsonic region shape is different as far forward as the plume locations. There is also an

interaction with the outflow boundaries along the side of the computational domain. Since the high thrust coefficient creates a larger effective body for the freestream flow, more space is needed in the lateral direction to account for the flow passing around the jet plumes.

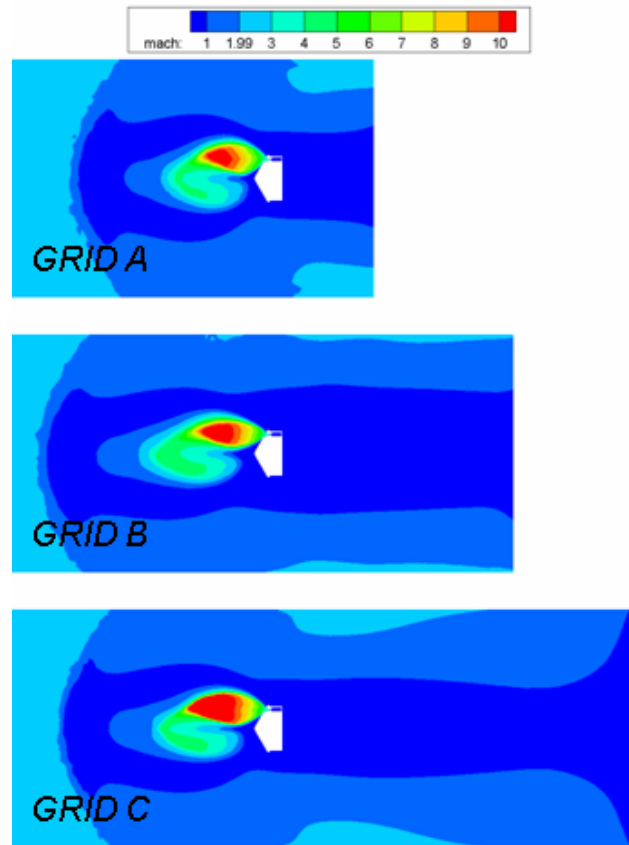


Figure 27: Exit Plane Effects on $C_T = 7.0$ Mach Contours for Peripheral Flow Structures

Though grid D isn't shown in Figure 27, the solution indicates that moving the exit plane far aft of the vehicle removes the subsonic wake interaction with the exit plane. This may not be known initially for a given supersonic retropropulsion configuration, but it should be checked to prevent potential boundary condition issues from affecting the flow field around the vehicle.

Higher Resolution CFD Solutions

In order to investigate the significant differences in jet flow structure amongst the preliminary grids, a finer resolution grid is generated with Gridgen V15.15. The exit plane and side boundaries of the computational domain are consistent with grid D. This grid has tetrahedral cells with anisotropic spacing in the nozzles, pentahedral cells for the vehicle boundary layer, and tetrahedral cells within the remaining computational volume. The grid contains 19.4 million nodes, an order of magnitude increase from the preliminary solutions.

Flow Structure—The flow field structures for a subset of the thrust conditions run are seen in Figure 28. The $C_T = 1.0$ solution resembles that seen for the preliminary grids, with a slightly underexpanded jet plume which does not disturb the bow shock inboard of the nozzles. The Mach contours are sharper for this grid, which is a function of the increased resolution in the plume region.

The $C_T = 4.0$ solution shows significant asymmetry in the flow field. The image shown in Figure 28 is the flow from one nozzle, which shows a secondary plume cell forming after the jet terminates. The secondary plume cell varies significantly for each nozzle and is most likely the source of the asymmetry. It is unknown if the asymmetry is a representation of a physical aspect of this thrust condition, or if it is a function of the local time stepping used to generate the solution. Thrust coefficients of 3.0 and 5.0 show some asymmetry, but not to the extent seen for $C_T = 4.0$. The residuals for this solution show a ringing behavior with a mean that is not decreasing. This potentially indicates unsteadiness in the flow field, though again this may also be an artifact of the local time stepping since it does not capture the time accurate history of the oscillation. This behavior is not seen in other recent work on the same geometry [7]. Those results do show the secondary plume cell forming, but the jet terminal shock is not as sharp along the inboard expansion as is shown in Figure 28. This does not appear to be an artifact of grid resolution, as preliminary grid D also showed the asymmetric behavior.

As the thrust coefficient is increased to $C_T = 7.0$, the flow field structure becomes steady again, and the plumes from each nozzle have the same shape. There is a remnant of the secondary plume cell in the solution, but it is not as pronounced as for the $C_T = 4.0$ solution. This flow structure closely resembles that seen in previous computational efforts [6], [7]. This solution also differs dramatically from preliminary grids A-C, which showed significant jet interaction, but agrees well with the shape seen in grid D in Figure 22.

For $C_T = 10.0$, significant jet interaction is seen in the higher resolution grid. Though not shown, the $C_T = 10.0$ solution on preliminary grid D shows no jet interaction but instead shows a larger plume similar in shape to that seen for $C_T = 7.0$. This discrepancy indicates that increasing grid resolution has a dramatic effect on the flow field structure. It is unknown which structure is expected at this condition since there is no corresponding wind tunnel data available, but jet coalescence is not unexpected since the jet plumes should eventually expand enough to interact inboard of the nozzles. The flow structure with coalescence begins to resemble a single plume with a termination shock, which causes the bow shock to be located further from the vehicle. This also affects the surface pressure, causing it to drop significantly across the forebody.

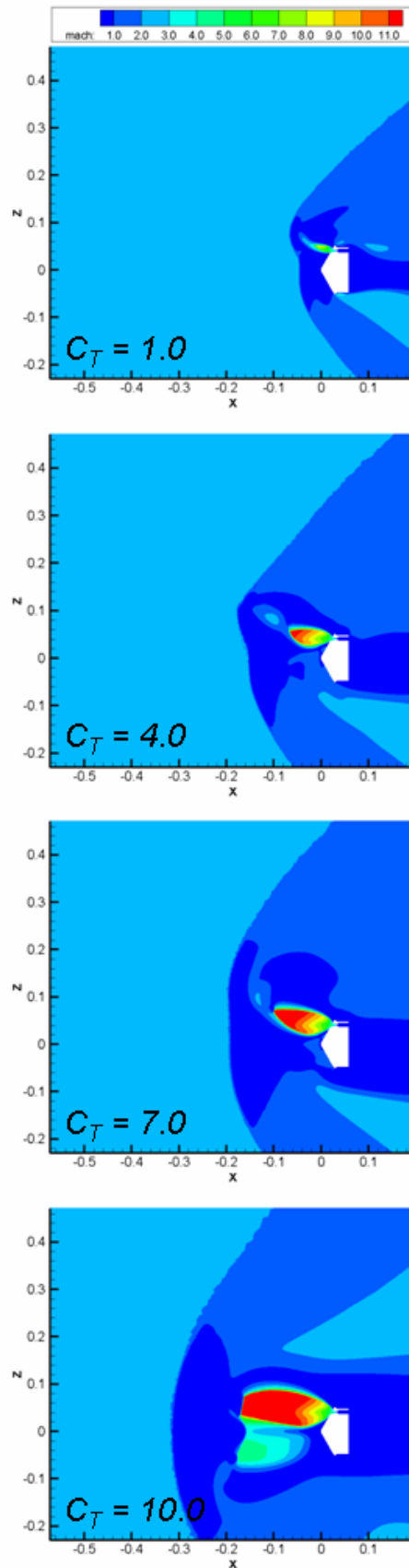


Figure 28: Flow Field Structures for the Higher Resolution Peripheral Configuration Grid

A comparison of the bow shock and jet terminal shock standoff distances is shown in Figure 29 for each thrust coefficient run on the higher resolution peripheral grid. The bow shock locations represent the position along the vehicle axis. The jet terminal shock location is more difficult to compare, as there is no clear distance to measure since the terminal shock covers a wide range of x locations. An average location is reported from the CFD simulations, which may only be order of magnitude comparable to the wind tunnel results since it is unclear how those distances were measured. Two trends are shown; one where each subsequent thrust coefficient uses the solution from the next lowest C_T value as an initial flow field (increasing thrust) and one where each thrust coefficient is restarted from the solution for the next highest C_T value (decreasing thrust). The decreasing thrust solutions will be discussed in the Solution Issues section. The increasing thrust solutions represent the data from the runs shown in Figure 28. In general, the jet standoff distances for these conditions agree favorably with the wind tunnel results. These jet plumes show no coalescence until $C_T = 10.0$, when the standoff distances increase noticeably. The plume coalescence causes the jet structure to resemble more of a single jet plume, and the standoff distances increase due to the interaction inboard of the nozzle exits.

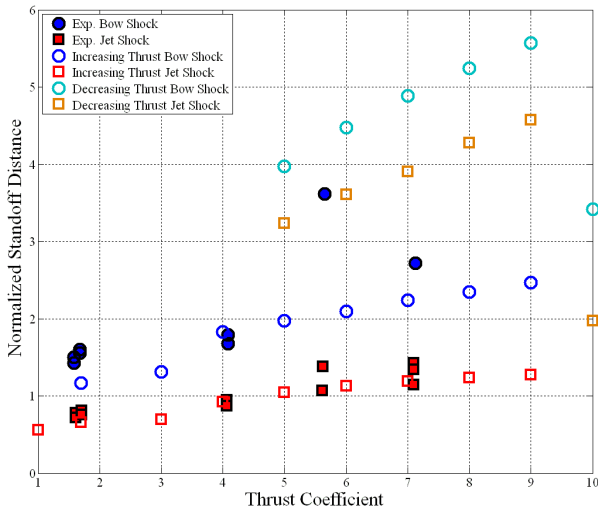


Figure 29: Flow Feature Standoff Comparison for Higher Resolution Peripheral Grid

Aerodynamics—Integrated drag coefficient trends are shown in Figure 30 for the range of thrust coefficients simulated. As with the flow feature locations, the increasing thrust data corresponds to the flow fields shown in Figure 28 and the pressure distributions shown in Figure 31. Except for $C_T = 10.0$, no plume coalescence is seen in these solutions. Thus the drag does not decrease as much as the wind tunnel data suggests it should since more pressure is preserved inboard of the nozzles than was reported. In general, as thrust coefficient increases and the plume expansion becomes larger, the drag coefficient plateaus since the pressure is being reduced to a roughly constant and low value across the entire forebody.

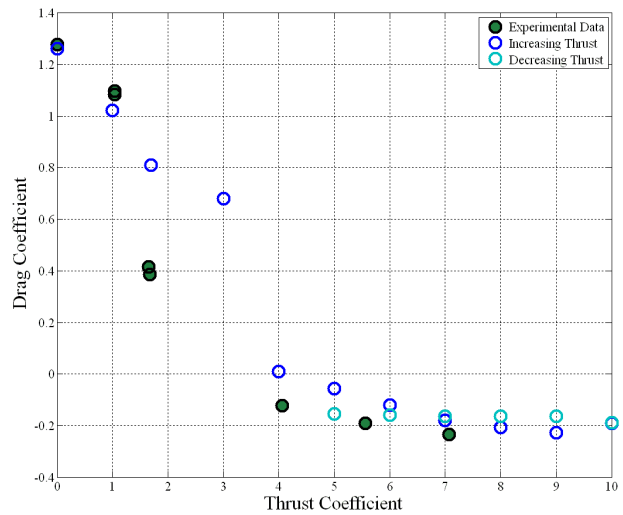


Figure 30: Integrated C_D Comparison for Higher Resolution Peripheral Grid

Pressure distributions for the same subset of thrust conditions as shown for the flow field structures are shown in Figure 31. As thrust increases, the level of pressure preserved on the forebody decreases as expected for increasingly expanded jet plumes. The $C_T = 1.0$ solution resembles that of the preliminary grids, indicating that low thrust coefficients appear to be more robust to grid resolution, which makes sense because the expansion of these jet plumes is small. For $C_T = 4.0$, the unsteadiness in the flow solution is evident in the asymmetric pressure distribution. Again, it is not expected for this to occur, and it is thought to be an artifact of the local time stepping approach used for these solutions. This pressure distribution is not in agreement with past works, which show a symmetric pressure distribution about each nozzle [7]. As thrust is further increased, the pressure distribution again becomes symmetric about each nozzle. For $C_T = 7.0$, some pressure is still preserved inboard of the nozzles, while the $C_T = 10.0$ solution shows a constant forebody pressure, consistent with previous observations on the effect of jet coalescence on the pressure distribution. This result agrees with grid D from the preliminary study for $C_T = 7.0$; however this is a different result at $C_T = 10.0$. Grid D in the preliminary study shows no plume coalescence, thus some pressure is still preserved.

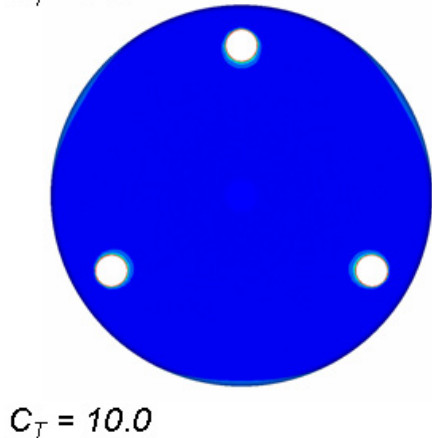
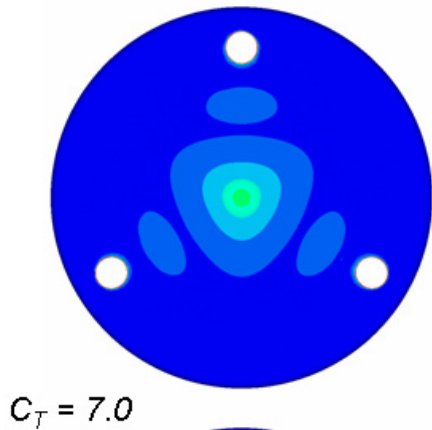
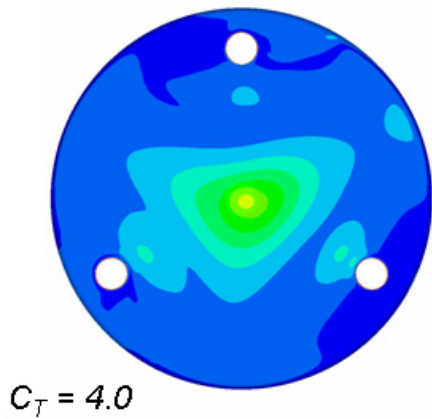
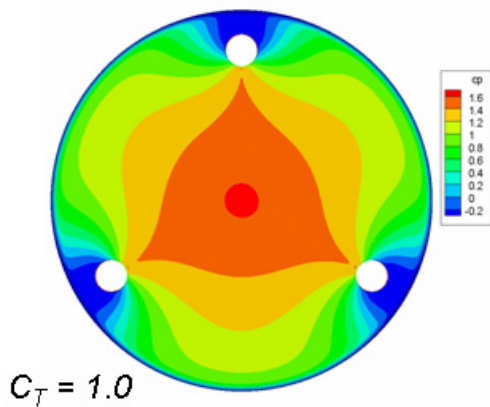


Figure 31: C_p Distributions for the Higher Resolution Peripheral Configuration Grid

Solution Issues—As mentioned previously, the primary issue noticed in these solutions is that the type of flow structure and pressure distribution seen on the vehicle depends on how the solution is initiated. The general method for generating solutions has been to first generate a low thrust solution with what should be a small jet plume. This solution should behave well since the plume expansion is not large and does not interact substantially with the bow shock. Then the next solution is restarted with the previous solution as an initial flow field from which FUN3D begins iterating toward the new solution. For the central configuration, this method showed no problems, as there is only one jet plume and the general plume structure remains the same. For the peripheral configuration, it has been shown that the flow structure used to initialize the solution has a drastic effect on the final flow field and pressure distribution. The data points labeled as “Increasing Thrust” in Figure 29 and Figure 30 use the next lowest thrust coefficient solution as the initial condition for the current thrust (i.e. $C_T = 7.0$ is restarted from $C_T = 6.0$). The data points labeled as “Decreasing Thrust” use the next highest C_T solution as the initial condition (i.e. $C_T = 8.0$ is restarted from $C_T = 9.0$). When the plumes coalesce at $C_T = 10.0$, this causes a hysteresis to occur in the flow fields; remnants of the coalescence remain in the flow field as thrust is decreased from $C_T = 10.0$. A sample effect on the pressure distribution is shown in Figure 32 for $C_T = 7.0$, and the full effect on the flow field for the thrust conditions run is shown in Figure 33.

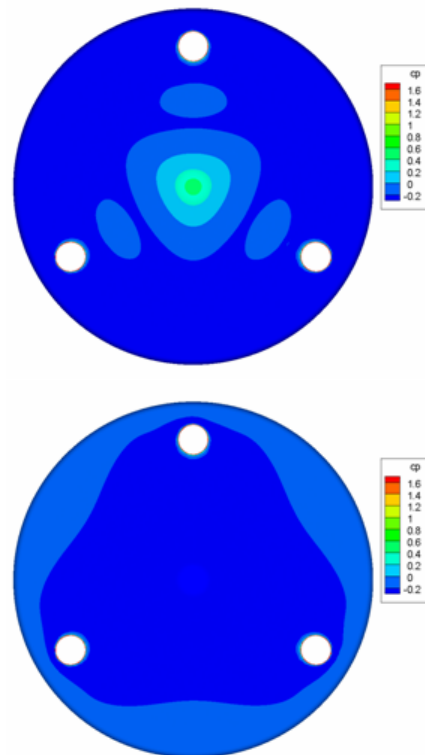


Figure 32: $C_T = 7.0$ Pressure Distribution Comparison between No Coalescence (top) and Coalescence (bottom)

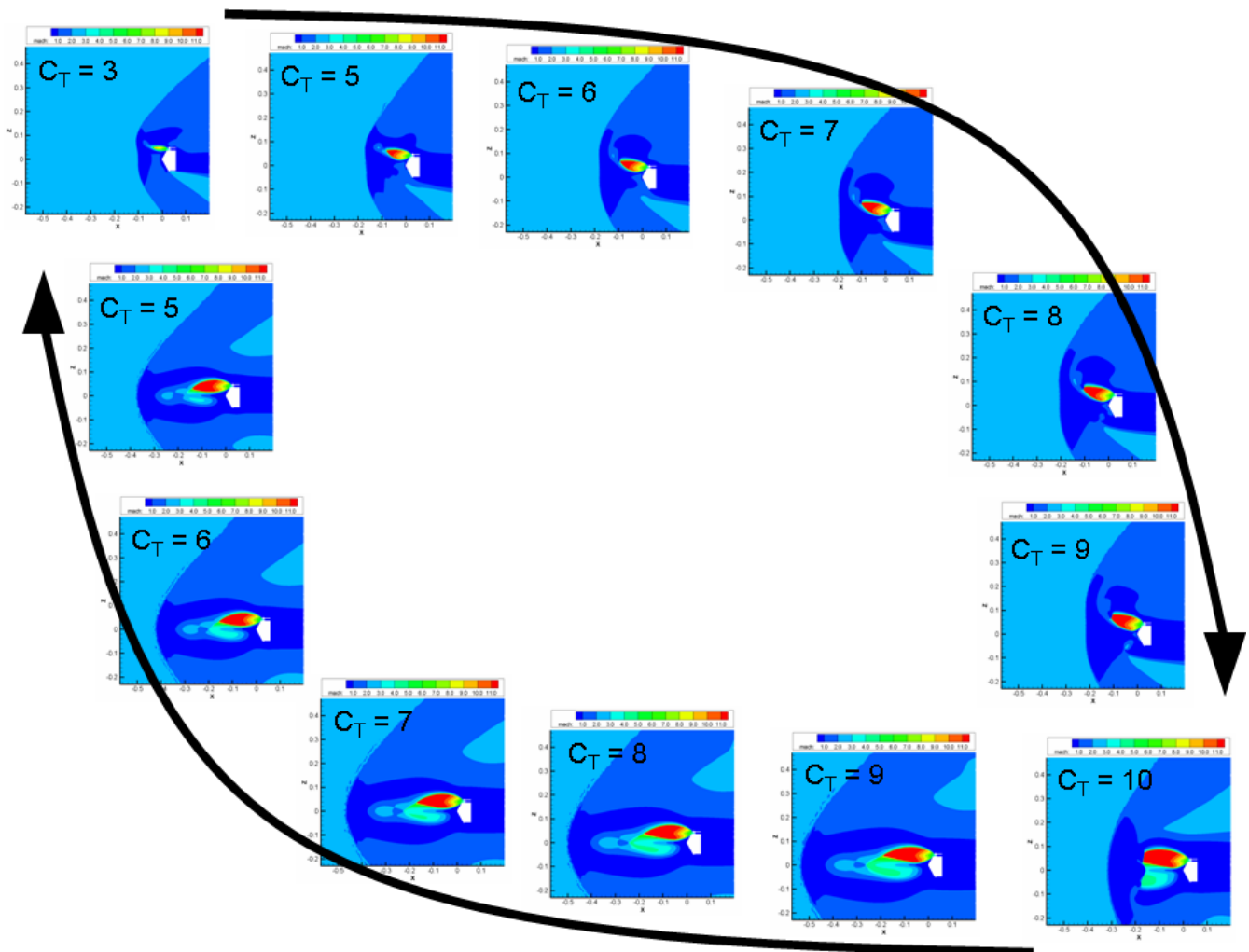


Figure 33: Plume Hysteresis for Varying Thrust Coefficients from $C_T = 3.0$ to $C_T = 10.0$

When the jets coalesce, as occurs for the “Decreasing Thrust” trends, the pressure on the body is completely lost due to the shielding provided by the jet plumes, as shown in Figure 32 for $C_T = 7.0$. The solution where each plume remains independent of each other shows the higher pressure preserved inboard of the nozzles, as shown for a range of C_T values in Figure 31. Understanding which plume structure should be seen, or under what conditions each occurs if both are possible, is important because the aerodynamic characteristics vary significantly. As is shown in Figure 30, the integrated drag coefficients are different for the varying plume structures. For some thrust coefficients, such as $C_T = 5.0$, the drag is higher for the independent plumes because significant pressure is preserved inboard of the nozzles. For other thrust coefficients, such as $C_T = 9.0$, the drag is higher for the coalesced plumes due to the higher pressure along the periphery of the vehicle. It is unclear from the current study if the hysteresis is only a numerical phenomenon, or if it has some physical basis. Further investigation is required to determine how varying thrust would impact the flow field and if the hysteresis could potentially affect an actual flight vehicle.

6. CONCLUSIONS

Supersonic retropropulsion provides a technology which can potentially enable higher mass systems to descend in low atmosphere environments. The flow field created by an SRP system is complex and varies greatly with configuration. A single nozzle located on the axis of the vehicle exhibits a jet plume whose expansion depends on the thrust desired from the rocket. The jet plume terminates in a Mach disk, and the bow shock inherent with supersonic speeds is pushed further from the vehicle body than is seen for vehicles with no rockets firing into the flow. As a consequence of the bow shock location changing, the pressure on the forebody decreases substantially, meaning that the primary deceleration force is the thrust from the rocket. A peripheral configuration exhibits a different flow structure, as each plume is bent away from the vehicle centerline. The plumes in this scenario resemble more of a jet in crossflow, since the decelerated flow through the bow shock turns to follow the forebody shape. This configuration has potential to preserve pressure along the forebody, thereby providing some aerodynamic drag in addition to the thrust from the nozzles.

The ability of CFD to capture the flow physics for SRP is greatly dependent on the grid used for the simulation. If the grid is too coarse, the solution may not be a good first approximation, as the plume will not form correctly. The jet boundary will appear more rounded and the Mach disk will not form for a central configuration. For a peripheral configuration, the amount of expansion for each jet is also tied to the grid resolution. The presence of jet interaction is dependent on the inboard expansion of the plumes, which also affects the pressure preserved on the forebody. Correctly modeling the inboard expansion of a peripheral configuration is essential for understanding the potential aerodynamic benefits inherent with nozzles located off the centerline. Additionally, the location of the exit plane can significantly affect the solution generated in a CFD simulation. If the exit plane is at the shoulder, the boundary condition needs to be verified to ensure that non-physical phenomena are not occurring at the exit plane. Even then, it may not be possible to obtain a second order accurate system, as the flow may still be changing at the exit plane. Offsetting the exit plane back from the vehicle helps, though care must be taken to ensure that the exit plane is not able to affect the vehicle aerodynamics. Since the retropropulsion flow field creates an effectively larger body to the oncoming freestream, the wake region behind the vehicle is much longer than for the model with no jets firing. The exit plane needs to be far enough back to fully encompass the subsonic region of the wake to ensure that no information can travel forward to the vehicle.

Taking into account grid resolution and exit plane location, it is possible to build a grid such that a wide range of thrust coefficients can be examined on a single grid. For the central configuration, there are two main modes which can be captured in the CFD simulation. For low thrust coefficients, a jet penetration mode exists where the jet does not terminate in a Mach disk, instead extending further upstream of the nozzle exit. This causes the bow shock to be located further from the body as well. The other mode, characterized by the jet terminating in a Mach disk, results in increasing the terminal shock and bow shock standoff distance as thrust increases. Since there is potential for high standoff distances at both low and high thrust coefficients, increased resolution is not just a function of the highest thrust run. The grid resolution is not wasted for a handful of cases, but rather provides support across a wide range of thrust conditions. For the peripheral configuration, the pressure on the forebody is preserved for a wide range of thrust coefficients, though the amount of pressure preserved decreases as thrust increases. The amount of inboard expansion is important to capture to determine the correct amount of pressure preservation, though one grid does seem capable of modeling a wide range of thrust conditions for this configuration as well. Additionally, it has been shown that the manner in which a solution is initialized has an effect on the flow solution, as there is potential for hysteresis to occur when the plumes coalesce in a previous solution. Plume coalescence can remain in subsequent

solutions if a solution with interaction is used as an initial condition.

7. FUTURE WORK

For the central configuration, the CFD simulations agree favorably with the experimental data. However, this is only obtained for one particular set of solver parameters. An investigation into different turbulence models, flux equations, and flux limiters may provide information as to which settings are particularly apt for modeling an SRP flow field. Additionally, the jet penetration mode is not as well captured as is expected from the experimental results. Further efforts to increase grid resolution in the jet penetration region may show this to be captured to a greater degree.

For the peripheral configuration, a higher resolution grid is required to determine the jet interaction effects for higher thrust coefficients. Based on the single nozzle grid resolution effects, the current peripheral grid may be too coarse to be adequately capturing the jet expansions. In particular, a range of thrust coefficients showed to be unsteady warrant investigation to determine if that is a function of the grid resolution or the flow field itself. Increases in the grid resolution should resolve the discrepancy seen between the CFD simulations and wind tunnel data in the forebody pressure and integrated drag at increased thrust coefficients. Additionally, further work is necessary to determine if the hysteresis seen in the flow solutions is a numerical artifact of local time stepping, or if there is some physical basis for the permanence of plume coalescence for varying thrust coefficient.

REFERENCES

- [1] Braun, R. D., and Manning, R. M., "Mars Exploration Entry, Descent, and Landing Challenges," *Journal of Spacecraft and Rockets*, Vol. 44, No. 2, pp. 310-323, March-April 2007.

- [2] Jarvinen, P. O., and Adams, R. H., "The Aerodynamic Characteristics of Large Angled Cones with Retrorockets," NASA CR NAS 7-576, February 1970.
- [3] McGhee, R. J., "Effects of a Retronozzle Located at the Apex of a 140° Blunt Cone at Mach Numbers of 3.00, 4.50, and 6.00," NASA TN D-6002, January 1971.
- [4] Daso, E. O., Pritchett, V. E., and Wang, T. S., "The Dynamics of Shock Dispersion and Interactions in Supersonic Freestreams with Counterflowing Jets," AIAA Paper 2007-1423, January 2007.
- [5] Peterson, V. L., and McKenzie, R. L., "Effects of Simulated Retrorockets on the Aerodynamic Characteristics of a Body of Revolution at Mach Numbers from 0.25 to 1.90," NASA TN D-1300, May 1962.
- [6] Korzun, A. M., Cordell, Jr., C. E., and Braun, R. D., "Comparison of Inviscid and Viscous Aerodynamic Predictions of Supersonic Retropropulsion Flowfields," AIAA Paper 2010-5048, June 2010.
- [7] Trumble, K. A., Schauerhamer, D. G., Kleb, W. L., Carlson, J.-R., Buning, P. G., Edquist, K. T., and Barnhardt, M. D., "An Initial Assessment of Navier-Stokes Codes Applied to Supersonic Retro-Propulsion," AIAA Paper 2010-5047, June 2010.

worked on conceptual IAD system design, entry flight mechanics trades, and the development of fluid-structure interaction codes capable of predicting the behavior of flexible decelerators.



Robert D. Braun is the David and Andrew Lewis Associate Professor of Space Technology in the Daniel Guggenheim School of Aerospace Engineering at the Georgia Institute of Technology and currently holds the position of NASA Chief Technologist. As Director of Georgia Tech's Space Systems Design Laboratory, he leads a research program focused on the design of advanced flight systems and technologies for planetary exploration. He is responsible for undergraduate and graduate level instruction in the areas of space systems design, astrodynamics, and planetary entry. Prior to coming to Georgia Tech, he served on the technical staff of the NASA Langley Research Center for sixteen years, where he contributed to the design, development, test, and operation of several robotic space flight systems. He has worked extensively in the areas of entry system design, planetary atmospheric flight, and mission architecture development. Dr. Braun is an AIAA Fellow and the principal author or co-author of over 150 technical publications in the fields of planetary exploration, atmospheric entry, multidisciplinary design optimization, and systems engineering. He has a B.S. in Aerospace Engineering from Penn State University, a M.S. in Astronautics from George Washington University, and a Ph.D. in Aeronautics and Astronautics from Stanford University.

BIOGRAPHY



Chris Cordell is currently a 4th year Graduate Research Assistant in the Space Systems Design Laboratory at the Georgia Institute of Technology. He holds a B.S. degree and an M.S. degree in Aerospace Engineering from the Georgia Institute of Technology. He has two summers of intern experience at NASA Langley Research Center and one summer of

experience at NASA Ames Research Center, where he gained familiarity with the CFD codes FUN3D and US3D, and performed analysis of supersonic retropropulsion with both codes in support of his graduate studies.



Ian Clark is a visiting assistant professor at the Georgia Institute of Technology and an employee of the Jet Propulsion Laboratory. He received his PhD from the Georgia Institute of Technology, where he also received his BS and MS. Ian's current research involves developing and maturing IADs for use during atmospheric entry. As part of this research, Dr. Clark has

